THE JOURNAL OF PHYSICAL CHEMISTRY B
A JOURNAL OF THE AMERICAN CHEMICAL SOCIETY

pubs.acs.org/JPCB

Article

Effects of Nanoconfinement on Dynamics in Concentrated Aqueous Magnesium Chloride Solutions

Samantha T. Hung, Sean A. Roget, and Michael D. Fayer*

Cite This: J. Phys. Chem. B 2024, 128, 5513−5527

Read Online

ACCESS | Metrics & More | Article Recommendations | Supporting Information

ABSTRACT: Water behavior in various natural and manufactured settings is influenced by confinement in organic or inorganic frameworks and the presence of solutes. Here, the effects on dynamics from both confinement and the addition of solutes are examined. Specifically, water and ion dynamics in concentrated (2.5−4.2 m) aqueous magnesium chloride solutions confined in mesoporous silica (2.8 nm pore diameter) were investigated using polarization selective pump−probe and 2D infrared spectroscopies. Fitting the rotational and spectral diffusion dynamics measured by the vibrational probe, selenocyanate, with a previously developed two-state model revealed distinct behaviors at the interior of the silica pores (core state) and near the wall of the confining framework (shell state). The shell dynamics are noticeably slower than the bulk, or core, dynamics. The concentration-dependent slowing of the dynamics aligns with behavior in the bulk solutions, but the spectrally separated water-associated and Mg^{2+}-associated forms of the selenocyanate probe exhibit different responses to confinement. The disparity in the complete reorientation times is larger upon confinement, but the spectral diffusion dynamics become more similar near the silica surface. The length scales that characterize the transition from surface-influenced to bulk-like behavior for the salt solutions in the pores are discussed and compared to those of pure water and an organic solvent confined in the same pores. These comparisons offer insights into how confinement modulates the properties of different liquids.

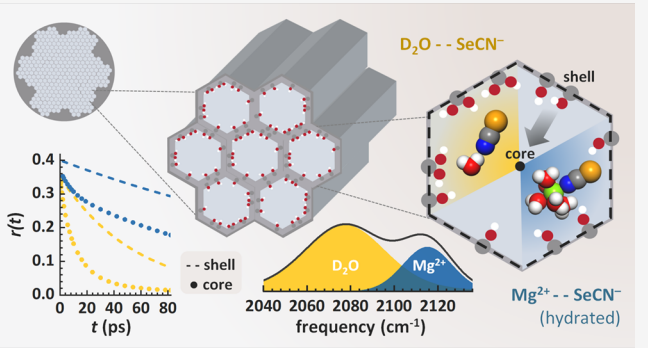

1. INTRODUCTION

Water is essential to the function and performance of many natural and artificial systems, in which solutes and confinement are common and can lead to dramatic deviations from bulk behavior. Confined aqueous electrolyte solutions in biological and chemical processes and energy storage materials are relevant to scientific and technological fields.[1−4] Aqueous magnesium solutions are particularly interesting as the magnesium cation, the most common divalent cation in intracellular fluids and seawater, has a remarkably high charge density.[5,6] Their liquid structure and dynamics are also relevant to the performance of emerging technologies such as magnesium-ion batteries.[7,8]

Researchers have been exploring the dynamics of confined water in materials such as porous silicas,[9−15] reverse micelles,[16−23] and fuel cell membranes.[24,25] MCM-41 is one type of mesoporous silica that has a hexagonal array of highly uniform and size-tunable cylinder-like pores, with pore diameters ranging from 1.5 to 10 nm.[26,27] These characteristics have made MCM-41 especially valuable in applications such as catalysis,[28,29] water treatment,[30,31] and drug delivery.[32,33] The understanding of aqueous salt solutions confined in MCM-41 has grown with recent investigations employing NMR,[34] X-ray,[35] and neutron scattering[36,37] techniques. Here, infrared (IR) polarization selective pump−probe (PSPP) spectroscopy and two-dimensional IR (2D IR) experiments were used to compare the rotational and spectral diffusion dynamics of bulk aqueous magnesium chloride ($MgCl_2$) solutions[38] with those confined in 2.8 nm MCM-41 pores. IR vibrational spectroscopy is well suited for studying molecular dynamics at picosecond time scales, complementing other spectroscopic techniques by offering more direct observation of how molecules move and interact with their immediate surroundings.

Liquid dynamics generally slow with confinement, and deviations from bulk behavior usually extend from the surface for a few molecular diameters, with the distance depending on surface−liquid and liquid−liquid interactions. The transition from the modified liquid behavior of the "shell" state near the surface of the confinement framework to the bulk-like behavior of the "core" state at the interior is often described by a two-state model of confined behavior.[39] A conventional two-state

Received: March 12, 2024
Revised: April 30, 2024
Accepted: May 3, 2024
Published: May 24, 2024

https://doi.org/10.1021/acs.jpcb.4c01639
J. Phys. Chem. B 2024, 128, 5513−5527

model defines a step discontinuity between the shell and core states. Modifications to the model account for more gradual transitions, the extent and shape of which are influenced by the nature of the confined liquid and surface moieties.[12,15,40,41]

We compared the effects of confinement in MCM-41 silica pores on three different liquids studied using the same selenocyanate ($SeCN^-$) probe: concentrated aqueous $MgCl_2$ solutions, pure water, and an organic solvent. The current study focuses on the $MgCl_2$ solutions (2.5−4.2 molal). Pure water[15] and 1-methylimidazole,[40] an organic solvent, were studied in prior work. In these previous studies, the confined rotational dynamics were described by an exponential acceleration from the shell state dynamics at the surface to the bulk-like dynamics at the core. In contrast, the confined spectral diffusion dynamics—representing structural fluctuations of the liquid—were described by more abrupt transitions between surface and core dynamics, behavior more akin to the conventional two-state model. Hydrogen bonding (H-bonding) and electrostatic interactions contributed to the slowing of the confined dynamics. Both interactions exist in the aqueous $MgCl_2$ solutions but can influence the dynamics of different species in solution to various extents. In the bulk $MgCl_2$ study, two $SeCN^-$ populations were observed.[38] The cation-associated $SeCN^-$ probe reported significantly slower dynamics, revealing differences in the local environments of the water and ionic species. We will discuss whether confinement exaggerates or reduces these differences and if concentration-dependent trends observed in the bulk are consistent with those in the pores. The widths of the shell layer characterizing the extent of the surface effects for the cation- and water-associated species will also be compared with those for the two other confined liquids.

Patterns induced by confinement will be elucidated by comparing the response of different liquids to confinement in the same hydrophilic MCM-41 pores. The findings will enhance our knowledge of confinement and contribute to advances in the design and functionality of mesoporous materials for applications in nanotechnology and energy storage.

2. EXPERIMENTAL METHODS

2.1. Sample Preparation and Linear IR Spectroscopy. Magnesium chloride ($MgCl_2$, anhydrous, >98%) from Sigma-Aldrich and deuterated water (D_2O, 99.9% D) from Cambridge Isotope Laboratories were used as received. The vibrational probe, potassium selenocyanate (KSeCN, 99%), from Acros Organics and the MCM-41 mesoporous silica from ACS Materials were vacuum-dried under heat to eliminate water (<100 mTorr, 60 °C for KSeCN and 200 °C for the silica) and stored in a nitrogen (N_2) glovebox. The pore diameter of the MCM-41 was determined to be 2.8 ± 0.1 nm using nitrogen sorption experiments.[15]

Different concentrations of aqueous $MgCl_2$ solutions (2.5, 3.1, and 4.2 molal) with the KSeCN probe (0.25 molal) were gravimetrically prepared and syringe filtered (0.22 μm) to remove particulate impurities. The $MgCl_2$ concentrations correspond to Mg^{2+} ion to D_2O mole ratios of 1−20, 1−16, and 1−12, with the highest 1−12 mole ratio (4.2 molal) being near saturation. MCM-41 silica powder was added to the filtered solution at ∼1 wt % silica and magnetically stirred for 15 min. Our established protocol for filling the silica mesopores without excess liquid outside the silica particles involves vacuum filtering off the excess liquid from the silica mixture and equilibrating the residue with the vapor of the liquid (e.g., water[42] and 1-methylimidazole[40]). However, $MgCl_2$ is so deliquescent[43,44] that the silica particles filled with $MgCl_2$ solution obtained after vacuum filtration turned from a macroscopically dry powder to a wet slurry upon exposure to the water vapor used for equilibration.

Consequently, a centrifugal filtration protocol was developed. A 450 μL aliquot of the silica mixture in a Nanosep centrifuge tube with a 300 K (molecular weight) membrane filter was centrifuged with an Eppendorf 5415D centrifuge under an N_2 atmosphere for 10 min at 16,100 rcf (13,200 rpm). After removing the filtrate, the inner tube containing the partially dried silica was rotated 180°. In the subsequent centrifugation step, the pellet was subjected to force in the opposite direction, allowing water trapped between silica particles to be exposed and removed. After another 10 min of centrifugation at 16,100 rcf, the sample (still in the inner tube) was sealed in a vial, transferred into an N_2 glovebox, and promptly placed and sealed in a sample cell with paraffin oil as an index matching fluid, as previously described.[42] The measured dynamics of the sealed sample remains unchanged for over a week. The optical path length of the sample was set with 25 μm Teflon spacers between two 25 mm diameter, 3 mm thick CaF_2 windows. Linear IR spectra of the samples with and without the KSeCN probe were taken with a Thermo Scientific Nicolet iS50 spectrometer with air free of CO_2 and H_2O.

The centrifugation parameters were optimized by comparing the dynamics of a diagnostic sample without $MgCl_2$, i.e., containing D_2O, KSeCN, and silica, with published results for confined water dynamics in identical 2.8 nm MCM-41 silica particles. The optimization was possible since the confined liquid dynamics are very sensitive to the level of pore filling. Results are shown in the Supporting Information (SI), along with the methodology for assessing the $MgCl_2$ concentration using ICP-MS and KF titration. Nitrogen sorption measurements[45] performed at the Soft & Hybrid Materials Facility (SMF) at the Stanford Nano Shared Facilities (SNSF) confirmed that the average pore diameter of the silica was unchanged after centrifugation.

2.2. Nonlinear IR Spectroscopy. The laser system has been discussed in detail.[46] The polarization selective pump−probe (PSPP)[47,48] and two-dimensional infrared (2D IR)[49,50] vibrational echo experiments, summarized below, were conducted following the methods described in our previous study of the bulk aqueous $MgCl_2$ solutions.[38]

The nonlinear IR experiments were performed using a pulse-shaping system configured in a pump−probe geometry. The CN stretch of the $SeCN^-$ probe was excited with mid-IR pulses centered at 2096 cm^{-1} that are ∼3 μJ at the sample. Phase cycling was implemented by precisely controlling the pump pulses with a germanium acousto-optic pulse shaper.[46,51,52] In the PSPP experiment, polarization-resolved transient intensity differences in the probe spectrum with and without the pump excitation were measured to give the time-dependent parallel $S_{\parallel}(t)$ and perpendicular $S_{\perp}(t)$ signals. The two signals were then used to construct the isotropic pump−probe decays $P(t)$ (eq 1) and the orientational anisotropy decays $r(t)$ (eq 2),[47,48] giving the vibrational lifetimes and orientational relaxation dynamics, respectively. The $r(t)$ is proportional to $C_2(t)$, the second Legendre polynomial orientational correlation function of the transition dipole moment along the CN bond.

https://doi.org/10.1021/acs.jpcb.4c01639
J. Phys. Chem. B 2024, 128, 5513−5527

$$P(t) = [S_{\|}(t) + 2S_{\perp}(t)]/3 \quad (1)$$

$$r(t) = \frac{S_{\|}(t) - S_{\perp}(t)}{S_{\|}(t) + 2S_{\perp}(t)} = 0.4C_2(t) \quad (2)$$

In the 2D IR vibrational echo measurements, a sequence of laser pulses interacts with the sample to record the initial (ω_1) and final (ω_3) frequencies of an ensemble of excited vibrational probe molecules. The ω_1 and ω_3 frequencies are the horizontal and vertical axes in a 2D spectrum. Changes in the vibrational frequency of a probe molecule within its inhomogeneously broadened absorption spectrum arise from changes in the local solvent structure that modify the probe-solvent intermolecular interactions. The waiting time, T_w, between the initial and final states is varied to track the time dependence of these frequency changes, i.e., spectral diffusion, and hence the time-dependent structural fluctuations. At short T_w, the 2D spectrum consists of an elongated 2D band shape along the $\omega_3 = \omega_1$ diagonal, indicating that ω_3 and ω_1 are strongly correlated. With increasing T_w, the band shape becomes progressively more round. This occurs because ω_3 (final frequencies) and ω_1 (initial frequencies) become increasingly decorrelated as the probe samples more solvent configurations, and correspondingly, more frequencies. The center-line-slope (CLS) method quantifies the time-dependent loss of correlation by analyzing a T_w series of 2D spectra.[53−55] The CLS obtained from the data is equivalent to the normalized frequency-frequency correlation function (FFCF), the probability that a vibrational probe with some initial frequency has the same frequency at T_w, averaged over all initial frequencies.[50,53−55]

Measurements can be conducted on the strongly light-scattering silica powder using polarization schemes, phase cycling techniques, and manipulation of incident beam intensities.[42,52,56,57] Still, only perpendicular polarization 2D spectra could be reliably measured in most commercially available mesoporous silica with particle diameters ranging from 10s to 100s of microns because of the scattered light contamination in the polarization parallel to the pump beam.[15,40] A four-shot phase cycle was also necessary to reduce heterodyne scatter in the pump−probe measurements.[42] However, the relatively small particle size (0.1−1 μm diameter) of the 2.8 nm MCM-41 used in this study resulted in little scatter, enabling the measurement of 2D spectra in both the parallel and perpendicular polarizations.

3. RESULTS AND DISCUSSION

3.1. Linear IR Absorption Spectra. Figure 1 shows the area-normalized, background-subtracted linear absorption spectra of $SeCN^-$ in confined aqueous $MgCl_2$ solutions of varying concentrations. As was previously observed in the bulk study of the same aqueous $MgCl_2$ solutions, there are two peaks centered at ∼2075 and ∼2115 cm^{-1}.[38] The lower frequency peak (2075 cm^{-1}) arises from the CN with its nitrogen lone pair hydrogen bonded to the OD of D_2O ("D_2O-associated peak"). This peak decreases in relative area with increasing salt concentration. The blue-shifted peak (2115 cm^{-1}) that grows in with increasing $MgCl_2$ concentration is from the CN with its nitrogen lone pair associated with Mg^{2+} ("Mg^{2+}-associated peak"). The center frequency and full width at half-maximum (FWHM) of each peak, obtained by fitting with two Voigt line shapes, are tabulated in Table 1 with the corresponding bulk values.

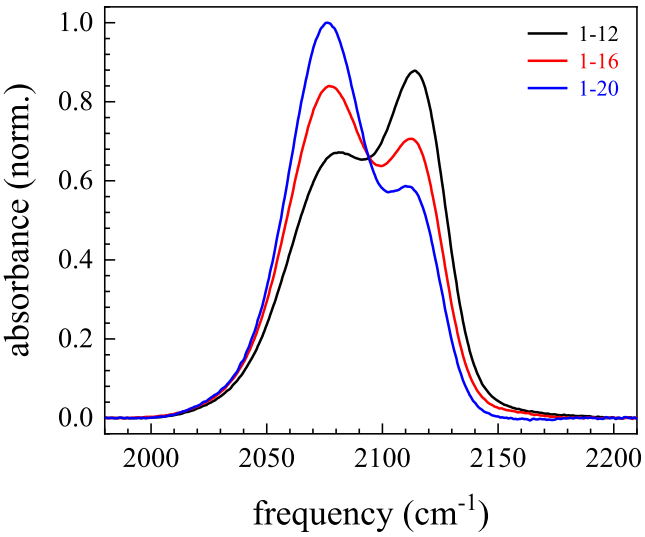

Figure 1. Linear IR spectra (area-normalized) of the CN stretch of $SeCN^-$ in aqueous $MgCl_2$ solutions with Mg^{2+} to D_2O mole ratios of 1−12, 1−16, and 1−20 confined in 2.8 nm silica pores. The D_2O-associated peak is centered at ∼2075 cm^{-1}. The higher frequency peak centered at ∼2115 cm^{-1} that grows with increasing salt concentration is the Mg^{2+}-associated peak.

The D_2O-associated peak blue shifts and broadens with increasing salt concentration. For pure D_2O, the center frequencies and FWHM are very similar for the bulk and confined systems. For the $MgCl_2$ solutions, the confined D_2O-associated peaks are slightly blue-shifted and have larger FWHM relative to the bulk. For the 1−16 mole ratio solution, the center frequency and FWHM in the bulk are 2076.2 ± 0.2 and 40.3 ± 0.2 cm^{-1}. The corresponding confined values are 2077.4 ± 0.3 and 44.8 ± 0.9 cm^{-1}. The Mg^{2+}-associated peak also broadens upon confinement, with a minimal (<1 cm^{-1}) blue shift in the center frequency. For the 1−16 solution, the bulk center frequency and FWHM are 2114.9 ± 0.1 and 24.7 ± 0.2 cm^{-1}. The corresponding pore values are 2115.3 ± 0.3 and 26.9 ± 0.1 cm^{-1}. The slight (∼1 cm^{-1}) variation in the center frequency across concentration may result from minor fitting errors in approximating the slightly asymmetric D_2O-associated peak[58] with a Voigt line shape.

The subtle differences in the bulk and pore peaks are primarily manifested as broader pore line shapes. Linewidth increase can result from inhomogeneous or homogeneous broadening. In the bulk study, the observed line broadening with increasing concentration was attributed to inhomogeneous broadening, which arises from increased variety in solvent configurations.[38] This was supported by the concentration independence of the homogeneous linewidths measured with 2D IR experiments. Since the bulk and pore homogeneous linewidths for each corresponding concentration are similar (Tables S3 and S4), it is likely that the line broadening observed in the pore also stems from inhomogeneous broadening.

In a prior study, confining 1-methylimidazole (MeIm), an organic solvent with a large dipole moment, within the same silica pores similarly led to inhomogeneous broadening of the $SeCN^-$ line.[40] This was linked to the electrostatic ordering of the MeIm dipoles by the silica surface. The ionic species in the $MgCl_2$ solution can also electrostatically interact with the charged silica surface, increasing the diversity of solvent−

https://doi.org/10.1021/acs.jpcb.4c01639
J. Phys. Chem. B 2024, 128, 5513−5527

Table 1. Line Shape Parameters and Vibrational Lifetimes

	D_2O-associated			Mg^{2+}-associated		
concentration (mole ratio)	center (cm^{-1})	FWHM (cm^{-1})	lifetime (ps)	center (cm^{-1})	FWHM (cm^{-1})	lifetime (ps)
bulk 1−12[a]	2078.1 ± 0.1	43.3 ± 0.1	23.5 ± 0.4	2115.8 ± 0.1	26.4 ± 0.1	30.1 ± 0.3
bulk 1−16[a]	2076.2 ± 0.2	40.3 ± 0.2	25.0 ± 0.3	2114.9 ± 0.1	24.7 ± 0.2	29.9 ± 0.1
bulk 1−20[a]	2075.4 ± 0.1	38.6 ± 0.1	26.3 ± 0.8	2114.9 ± 0.1	22.7 ± 0.4	29.8 ± 0.6
bulk D_2O[b]	2074.7 ± 0.1	32.9 ± 0.1	36.2 ± 0.1			
pore 1−12	2079.9 ± 0.5	49.5 ± 0.1	20.2 ± 0.4	2116.3 ± 0.1	28.1 ± 0.3	25.5 ± 0.1
pore 1−16	2077.4 ± 0.3	44.8 ± 0.9	20.6 ± 0.6	2115.3 ± 0.3	26.9 ± 0.1	25.5 ± 0.4
pore 1−20	2076.2 ± 0.5	41.8 ± 0.1	21.7 ± 0.4	2114.9 ± 0.1	25.0 ± 0.9	25.2 ± 0.3
pore D_2O[c]	2074.8 ± 0.4	31.5 ± 0.1	34.0 ± 0.2			

[a]ref 38. [b]ref 58. [c]ref 15.

solvent and solvent-probe interactions. These interactions affect the CN bond strength and, hence, the triple bond character of the nitrile stretch, resulting in a broader range of $SeCN^-$ vibrational frequencies.[59]

3.2. Vibrational Relaxation. While the D_2O- and Mg^{2+}-associated $SeCN^-$ peaks are visually distinguishable in the linear spectrum (see Figure 1), their third-order pump−probe signals interfere. The isolation of the D_2O- and Mg^{2+}-associated pump−probe signals follows the approach described in the bulk aqueous $MgCl_2$ study[38] and is discussed in the SI.

The isotropic signals $P(t)$ were constructed from the pump−probe signals using eq 1. The vibrational lifetimes for the CN stretch of D_2O- and Mg^{2+}-associated $SeCN^-$ (Table 1) were obtained by fitting the $P(t)$. The D_2O-associated $P(t)$ is biexponential due to the non-Condon effect, with the faster time constant corresponding to the equilibration of unevenly pumped, frequency-dependent transition dipoles via fast spectral diffusion (Section 3.4 discusses spectral diffusion).[38,58,60] The vibrational lifetime is the slower time constant, which is identical within error to the time constant obtained from fitting the $P(t)$ with a single exponential from 10 ps onward. The Mg^{2+}-associated lifetime is the time constant from a single exponential fit to the Mg^{2+}-associated $P(t)$.

The vibrational lifetimes for both species are frequency-independent. For the D_2O-associated peak, the lifetime (Table 1) decreases with increasing salt concentration, from 21.7 ps for the 1−20 solution to 20.2 ps for the 1−12 solution. These pore lifetimes are 2−4 ps shorter than their bulk counterparts. For the Mg^{2+}-associated peak, the pore lifetimes are about 5 ps shorter than the bulk lifetimes but identical across concentrations. A minor lifetime reduction was also observed in confined pure D_2O.[15] The lifetime reduction for the aqueous solutions is subtler than that for MeIm confined in the same pores and measured with the same $SeCN^-$ probe.[40]

The vibrational lifetime, determined by the coupling strength of a vibrational mode to other modes in the system, is a sensitive probe of the local solvent environment. Given that the CN stretch vibrational frequency is almost identical in the bulk and confined solutions, the frequencies of the intramolecular Se−C stretching and Se-CN bending modes are likely also unchanged. Since the energy of the CN stretching mode cannot be exactly matched by a combination of the intramolecular modes, its vibrational relaxation involves one or more solvent modes. The rate of energy deposition into these solvent modes depends on the intermolecular coupling and the density of states.[40,61,62] Thus, the shortening of the $SeCN^-$ lifetime in the confined aqueous $MgCl_2$ solutions involves more efficient energy transfer through stronger coupling, higher density of states, or both, which may result from stronger interactions between the anionic probe and the surrounding molecules inside the surface-charged silica pore. Local peaks in density are also common for confined liquids and have been linked to increased rates of vibrational relaxation.[40,63] The confinement effects likely do not propagate far from the surface as the changes in the vibrational lifetime are subtle. The impact of confinement on other dynamical variables will be explored in subsequent sections and the results will be juxtaposed with the behavior observed for confined MeIm and water.

3.3. Orientational Relaxation. The anisotropy decay $r(t)$ (eq 2) tracks the $SeCN^-$ orientational relaxation dynamics in the confined aqueous solutions. The $r(t)$ are frequency-independent near the line center for both D_2O- and Mg^{2+}-associated peaks. In Figure 2a, the frequency-averaged D_2O-associated $r(t)$ data (points) are fit with biexponential decays

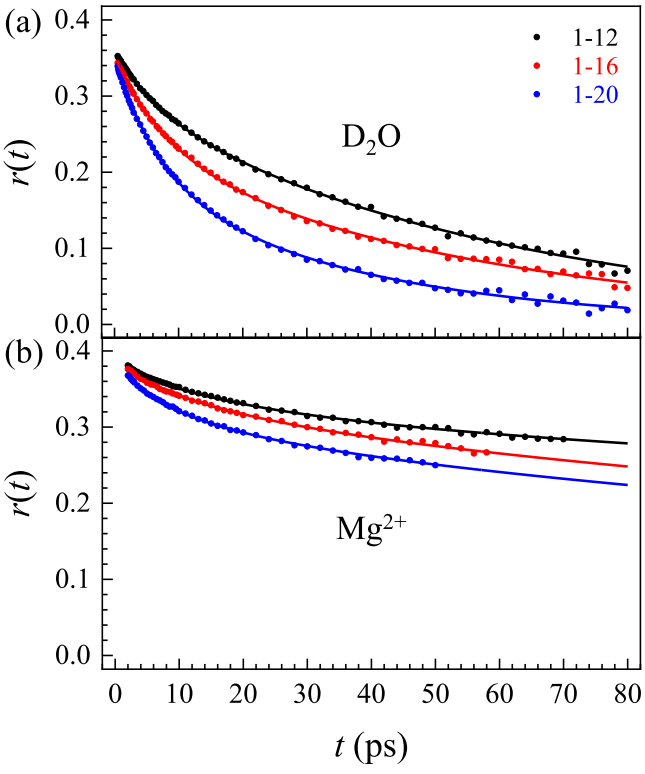

Figure 2. Measured rotational anisotropy $r(t)$ decays of $SeCN^-$ in aqueous $MgCl_2$ solutions of varying concentrations confined in 2.8 nm silica pores. (a) The solid curves are biexponential fits to the data for the D_2O-associated peak. (b) The solid curves are two-component fits to the data at the center frequency of the Mg^{2+}-associated peak.

https://doi.org/10.1021/acs.jpcb.4c01639
J. Phys. Chem. B 2024, 128, 5513−5527

Table 2. Orientational Relaxation Parameters (D_2O-Associated)[a]

bulk	A_1	t_1 (ps)	A_2	t_2 (ps)	A_3	t_3 (ps)	τ_c (ps)
bulk 1−12[b]	0.03 ± 0.01	2.7 ± 0.1	0.20 ± 0.01	13.5 ± 0.6	0.13 ± 0.01	67 ± 8	31 ± 2
bulk 1−16[b]	0.05 ± 0.01	2.4 ± 0.1	0.24 ± 0.01	11.4 ± 0.1	0.07 ± 0.01	54 ± 2	18 ± 1
bulk 1−20[b]	0.04 ± 0.01	1.9 ± 0.4	0.25 ± 0.01	8.6 ± 0.8	0.06 ± 0.01	39 ± 5	12.7 ± 0.5
bulk D_2O[c]	0.073 ± 0.002	1.4 ± 0.1	0.304 ± 0.003	4.5 ± 0.1			3.8 ± 0.1
pore[d]	A_1	t_1 (ps)		A_2	t_2 (ps)		τ_c (ps)
pore 1−12	0.06 ± 0.01	5 ± 1		0.31 ± 0.01	56 ± 3		48 ± 4
pore 1−16	0.11 ± 0.02	8 ± 1		0.24 ± 0.02	52 ± 5		39 ± 2
pore 1−20	0.16 ± 0.05	7 ± 2		0.19 ± 0.05	39 ± 6		23.9 ± 0.5
pore D_2O[e]	0.17 ± 0.02	2.5 ± 0.2		0.20 ± 0.02	7.6 ± 0.3		5.3 ± 0.1

[a]Multiexponential fit parameters to the anisotropy for $SeCN^-$ associated with D_2O in bulk and confined aqueous $MgCl_2$ solutions of varying concentrations. The A_i and t_i are the amplitude and time constant of the i^{th} component. [b]ref 38. [c]ref 58. [d]Because the pore t_2 values closely correspond to the bulk t_3 values, the pore A_2 and t_2 columns were placed below the bulk A_3 and t_3 columns. [e]ref 15.

Table 3. Orientational Relaxation Parameters (Mg^{2+}-Associated)[a]

	A_1	t_1 (ps)	A_2	t_2 (ps)	τ_c (ps)
bulk 1−12[b]	0.064 ± 0.007	15 ± 3	0.316 ± 0.008	226 ± 27	190 ± 18
bulk 1−16[b]	0.06 ± 0.02	8 ± 2	0.31 ± 0.02	148 ± 17	124 ± 8
bulk 1−20[b]	0.083 ± 0.002	7.4 ± 0.9	0.290 ± 0.006	119 ± 9	94 ± 7
pore 1−12	0.04 ± 0.01	16 ± 6	0.35 ± 0.01	463 ± 47	415 ± 28
pore 1−16	0.04 ± 0.02	17 ± 3	0.35 ± 0.02	287 ± 31	261 ± 26
pore 1−20	0.03 ± 0.02	13 ± 2	0.36 ± 0.02	247 ± 25	228 ± 19

[a]Fit parameters extracted from two-component fits to the anisotropy for $SeCN^-$ associated with Mg^{2+} in bulk and confined aqueous $MgCl_2$ solutions of varying concentrations. The A_i and t_i are the amplitude and time constant of the i^{th} component. [b]ref 38.

(solid curves, Table 2) with no offsets. The Mg^{2+}-associated $r(t)$, with interfering contributions from the overlapping D_2O-associated $r(t)$, are plotted in Figure 2b at the center frequency and fit with a two-component model (see SI for details). The Mg^{2+}-only $r(t)$'s isolated from the two-component fits decay as biexponentials to zero (no long time offsets) (Table 3). Directly fitting the Mg^{2+}-associated data, including the D_2O-associated contributions, using biexponentials ("direct fits," Table S1) gives the same slower decay time constant (t_2) as the two-component fits (Table 3) at every concentration. The difference is in the faster t_1, showing that the more rapidly decaying D_2O-associated $r(t)$ contributes only at early times. In both the bulk and the pore, the Mg^{2+}-associated dynamics are slower than the D_2O-associated dynamics, and all dynamics slow with increasing salt concentration.[38]

The bulk $r(t)$ decay of $SeCN^-$ in pure D_2O is biexponential. Slower versions of the two decay components were found in the D_2O-associated $r(t)$ of the bulk $MgCl_2$ solutions, which required a triexponential fit (Table 2).[38] The appearance of a third time constant with the addition of $MgCl_2$ reflects additional constraints on reorientation and associated changes in the liquid structure. However, the more slowly decaying D_2O-associated $r(t)$ in the confined $MgCl_2$ solutions are all biexponential. Notably, at every concentration, the slowest pore time constant (t_2) is the same within error as the slowest bulk time constant (t_3). For example, in both the bulk and confined 1−20 solution, the slowest time constant is 39 ps. The slowest time constant for an $r(t)$ that decays to zero corresponds to complete, unrestricted orientational relaxation. The similarity of these time constants suggests that the complete reorientation process is similar for the bulk and confined D_2O-associated $SeCN^-$. However, the relative amplitude associated with the slowest time constant as a percentage of the total $r(t)$ decay is much larger in the pore. In the bulk, orientational relaxation is dominated by faster, restricted angular diffusion processes, with the amplitudes (A_1 and A_2) corresponding to the two shorter time constants making up 60−80% (depending on the concentration) of the $r(t)$ decay. The absence of one of these shorter time constants in the pore may stem from the spatially averaged nature of the observed pore dynamics; i.e., the observed time constant t_1 may be an average of two short time constants. Alternatively, t_1 in the pore may correspond to one of the two restricted reorientation processes that occur in the bulk, suggesting the disappearance or suppression of the second process.

To compare the bulk and pore data across different functional forms, we introduce the integrated correlation time τ_c, which weights each time component by its normalized amplitude,

$$\tau_c = \frac{1}{A(0)}\int_0^\infty A(t)dt = \frac{1}{\sum_i A_i(0)}\int_0^\infty \sum_i A_i(0)e^{-t/t_i}dt \quad (3)$$

with $A(t)/A(0)$ representing the normalized correlation function of $C_2(t)$. For D_2O-associated dynamics in the most concentrated 1−12 solution, the pore τ_c is 48 ± 4 ps and the bulk τ_c is 31 ± 2 ps. The pore τ_c is larger for all concentrations measured.

As shown in Table 3, the integrated correlation time τ_c for the Mg^{2+}-associated dynamics increases with concentration from 94 to 190 ps in the bulk and from 228 to 415 ps in the pore. The slowing of the dynamics stems primarily from t_2, which exceeds t_1 by more than an order of magnitude for all samples. For every concentration, t_2 approximately doubles upon confinement. For the 1−20 solution, t_2 increases from 119 to 247 ps. In contrast, for the D_2O-associated orientational dynamics, the slowest time constant is unchanged upon confinement. The disparity suggests that the mechanism for complete reorientation is heavily influenced by confinement for Mg^{2+}-associated $SeCN^-$ but not for D_2O-associated,

https://doi.org/10.1021/acs.jpcb.4c01639
J. Phys. Chem. B 2024, 128, 5513−5527

reflecting different interactions of the two $SeCN^-$ species with the silica surface.

Overall, the pore rotational dynamics are substantially slower than the bulk. The distance dependence of the orientational relaxation will be discussed in Section 4, with the rotational dynamics interpreted as a weighted sum of a bulk and a distinctive shell component. The weighting of this shell component and its corresponding dynamics will provide additional insights into how confinement changes the aqueous $MgCl_2$ solution.

3.4. Spectral Diffusion. The 2D IR spectra of the nitrile stretch of $SeCN^-$ in three concentrations (1−12, 1−16, and 1−20) of confined $MgCl_2$ solutions are shown at T_w = 1.5 and 30 ps in Figure 3. All of the spectra are isotropic (i.e., constructed from parallel and perpendicular polarization 2D spectra) and report on the structural spectral diffusion dynamics.[64] The overlapping absorption bands are the D_2O-associated ($\omega_1 \sim 2075$ cm^{-1}) and Mg^{2+}-associated ($\omega_1 \sim 2115$ cm^{-1}) $SeCN^-$ species. Similar to the behavior observed in the bulk solution,[38] chemical exchange,[65,66] or the switching of the $SeCN^-$ probe between the D_2O- and Mg^{2+}-associated forms through dissociation and association, was not observed on the time scale of the experiment.

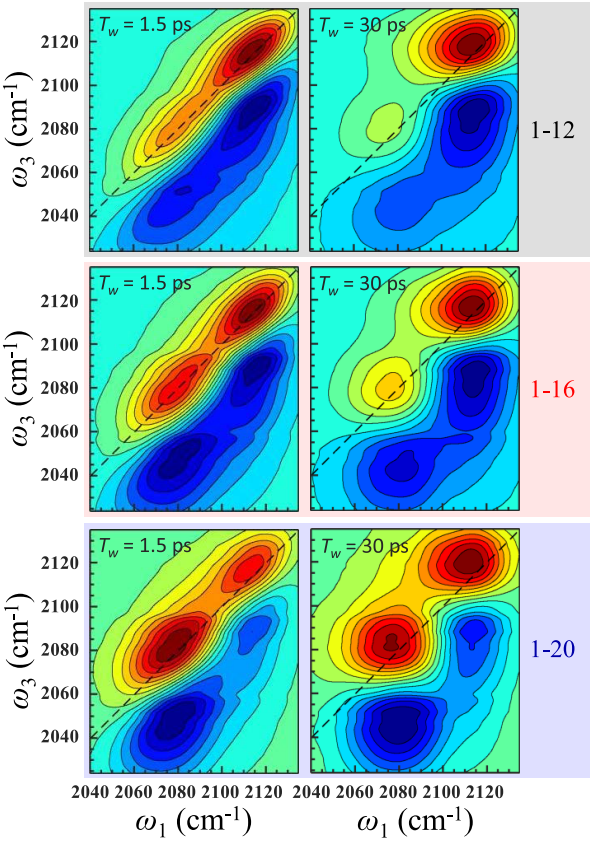

Figure 3. 2D IR spectra of the CN stretch of $SeCN^-$ in aqueous $MgCl_2$ solutions of varying concentrations confined in 2.8 nm silica pores at time delays T_w = 1.5 and 30 ps. The two red bands (0−1 vibrational transitions) on the diagonal (dashed line) arise from the D_2O- and Mg^{2+}-associated species. Each has a corresponding blue band (1−2 vibrational transition).

The CLS method used to analyze the 2D spectra relies on amplitude information within the absorption bands.[53−55] For spectra with bands from two or more species, the overlap of bands arising from the different species distorts the CLS.[67−69] The bands must be isolated to accurately extract the spectral diffusion dynamics of each $SeCN^-$ ensemble. To isolate the bands, the spectra were modeled with 2D Gaussian line shapes for each band (Figure S5), and the desired bands were isolated (Figure S6) by removing the extraneous bands from the experimental data.[69] Additional details are in the SI and the bulk study.[38] The isolated 0−1 transition bands correspond to the red, positive going peaks in the 2D spectra. The blue, negative going peaks are 1−2 transitions, which have the same ω_1 frequency as the corresponding 0−1 peaks but are shifted downward along ω_3 by the vibrational anharmonicity.

The shapes of the 0−1 transitions at a short time (T_w = 1.5 ps, Figure 3) are elongated along the diagonal, indicating a strong correlation between the initial (ω_1) and final (ω_3) frequencies (i.e., $\omega_1 \approx \omega_3$). The loss of correlation between ω_1 and ω_3 with increasing T_w results in rounder peaks (T_w = 30 ps, Figure 3). This change is tracked by an exponential decay of the CLS(T_w) values (Figure 4), which were extracted from a T_w series of 2D spectra. In Figure 4, biexponential (D_2O-associated) and triexponential (Mg^{2+}-associated) fits to the CLS decays (points), both with no offsets, are shown as solid lines. The corresponding fitting parameters are tabulated in Tables 4 and 5. These results exclude the D_2O-associated peak for the 1−12 sample, which is too weak (Figure 3) to be reliably resolved using the 2D Gaussian method described above. The CLS decay for pure D_2O confined in a 2.8 nm pore, previously fit with a triexponential in an earlier study,[15] was better fit with a biexponential; the biexponential fitting parameters are shown in Table 4.

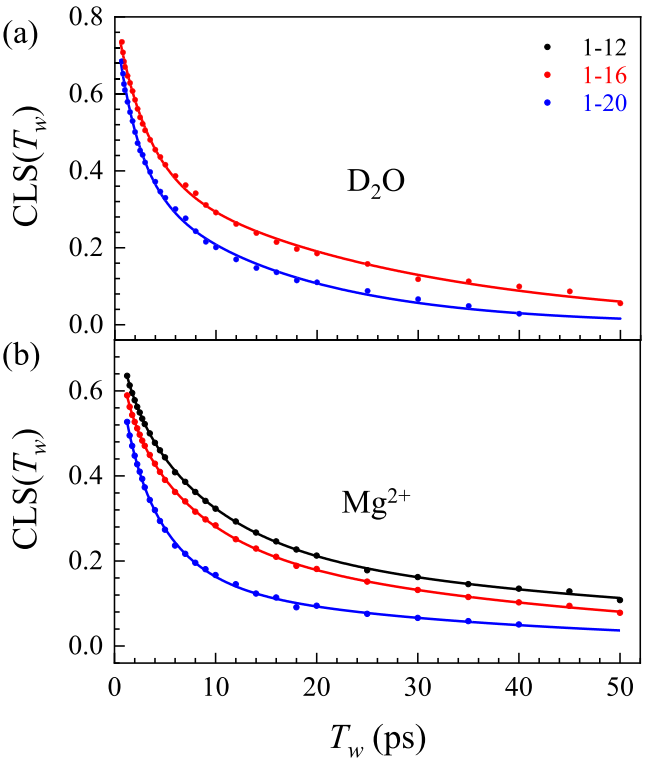

Figure 4. Measured CLS(T_w) decays (spectral diffusion) of $SeCN^-$ in aqueous $MgCl_2$ solutions of varying concentrations confined in 2.8 nm silica pores. (a) The solid curves are biexponential fits to the data for the D_2O-associated peak. (b) The solid curves are triexponential fits to the data for the Mg^{2+}-associated peak.

https://doi.org/10.1021/acs.jpcb.4c01639
J. Phys. Chem. B 2024, 128, 5513−5527

Table 4. CLS Parameters (D_2O-Associated)[a]

	A_1	t_1 (ps)	A_2	t_2 (ps)	τ_c (ps)
bulk 1−16[b]	0.42 ± 0.01	1.4 ± 0.2	0.25 ± 0.04	8 ± 1	3.8 ± 0.3
bulk 1−20[b]	0.43 ± 0.02	1.1 ± 0.1	0.23 ± 0.04	6 ± 1	2.9 ± 0.1
bulk D_2O[c]	0.25 ± 0.03	0.6 ± 0.1	0.31 ± 0.04	1.4 ± 0.2	1.0 ± 0.05
pore 1−16	0.41 ± 0.06	2.5 ± 0.2	0.43 ± 0.05	26 ± 4	14 ± 1
pore 1−20	0.37 ± 0.06	1.8 ± 0.4	0.38 ± 0.04	17 ± 2	9 ± 2
pore D_2O[d]	0.47 ± 0.03	0.9 ± 0.1	0.12 ± 0.02	4.4 ± 0.3	1.6 ± 0.1

[a]Biexponential fit parameters to the CLS for $SeCN^-$ associated with D_2O in bulk and confined aqueous $MgCl_2$ solutions of varying concentrations. The A_i and t_i are the amplitude and time constant of the i^{th} component. [b]ref 38. [c]ref 58. [d]ref 15. Data was refit to a biexponential (c.f., triexponential fit in the referenced publication).

Table 5. CLS Parameters (Mg^{2+}-Associated)[a]

	A_1	t_1 (ps)	A_2	t_2 (ps)	A_3	t_3 (ps)	τ_c (ps)
bulk 1−12[b]	0.20 ± 0.01	1.5 ± 0.1	0.37 ± 0.01	5.4 ± 0.2	0.11 ± 0.03	34 ± 1	9.0 ± 0.3
bulk 1−16[b]	0.24 ± 0.03	1.2 ± 0.2	0.34 ± 0.01	4.8 ± 0.5	0.08 ± 0.04	29 ± 4	6.4 ± 0.7
bulk 1−20[b]	0.22 ± 0.03	1.3 ± 0.3	0.31 ± 0.03	3.9 ± 0.2	0.07 ± 0.02	21 ± 5	4.9 ± 0.7
pore 1−12	0.13 ± 0.01	1.3 ± 0.3	0.40 ± 0.04	8 ± 2	0.25 ± 0.03	62 ± 9	24 ± 4
pore 1−16	0.16 ± 0.02	1.2 ± 0.1	0.34 ± 0.02	6.9 ± 0.5	0.25 ± 0.02	44 ± 5	18 ± 1
pore 1−20	0.15 ± 0.04	1.3 ± 0.3	0.42 ± 0.02	4.4 ± 0.4	0.16 ± 0.03	35 ± 7	11 ± 1

[a]Triexponential fit parameters to the CLS for $SeCN^-$ associated with Mg^{2+} in bulk and confined aqueous $MgCl_2$ solutions of varying concentrations. The A_i and t_i are the amplitude and time constant of the i^{th} component. [b]ref 38.

Like the rotational dynamics, the spectral diffusion dynamics slow with increasing salt concentration, and the Mg^{2+}-associated dynamics are slower than the corresponding D_2O-associated dynamics. Spectral diffusion also slows significantly upon confinement. The τ_c for the D_2O-associated peak (Table 4) is three to four times slower in the 2.8 nm silica pores. In pure D_2O, the change is less than a factor of 2. The pore Mg^{2+}-associated τ_c (Table 5) is about two to three times slower than the bulk τ_c. For the 1−16 solution, the τ_c is 14 vs 3.8 ps for the D_2O-associated peak and 18 vs 6.4 ps for the Mg^{2+}-associated peak. While the number of time constants for corresponding bulk and pore CLS decays is unchanged upon confinement, the D_2O-associated time constants (t_1 and t_2) in the pore are larger than those in the bulk, as are the two slower Mg^{2+}-associated time constants (t_2 and t_3). There is also a general shift in amplitudes from the faster to the slower time components upon confinement. Thus, under confinement, the slower processes become slower and contribute more to spectral diffusion.

As mentioned in Section 2.2, the CLS is the normalized FFCF. The CLS and the FFCF have the same time constants t_i. While the amplitudes in the CLS are normalized, the amplitudes Δ_i in the FFCF are in absolute frequency units (cm^{-1}) and quantify the extent of frequency fluctuations of the corresponding spectral diffusion processes. In addition, the FFCF provides the homogeneous component of the dynamics. The complete FFCF is described by the Kubo model:[50,70]

$$\mathrm{FFCF} = \langle \delta\omega(T_w)\delta\omega(0)\rangle = \frac{\delta(T_w)}{T_2} + \sum_i \Delta_i^2 \exp(-T_w/t_i) \quad (4)$$

The frequency fluctuation $\delta\omega(T_w)$ represents the difference between the average frequency $\langle\omega\rangle$ and the instantaneous frequency $\omega(T_w)$ of the vibrational probe. $\delta(T_w)$ is the Dirac delta function and T_2 is the total homogeneous dephasing time. The i^{th} decay process is characterized by the amplitude of the frequency fluctuation Δ_i and the time constant t_i. Using the CAFE program, the spatially averaged FFCF parameters (Tables S3 and S4) can be calculated from the spatially averaged pore CLS and the linear spectra.[55] It is not straightforward to decompose the FFCF into shell and core components, as the linear spectra of the confined solutions do not exhibit distinct shell and core distributions.

Calculating the FFCF parameters involves separating the absorption line into homogeneous and inhomogeneous contributions.[50] The total inhomogeneous linewidth is the convolution of the individual Gaussian inhomogeneous components. It is given by $\mathrm{FWHM} = 2(2\ln 2)^{1/2}\Delta_{total}$, where $\Delta_{total} = (\sum_i \Delta_i^2)^{1/2}$, where Δ_i are the standard deviations of the Gaussian components. The observed total homogeneous (Lorentzian) linewidth is $\Gamma = 1/(\pi T_2)$, which differs from the pure dephasing linewidth Γ^* as the observed dephasing time T_2 includes contributions from the vibrational lifetime T_1 and the orientational relaxation time T_{or} ($1/T_2 = 1/T_2^* + 1/2T_1 + 1/3T_{or}$).[53] The pore homogeneous linewidths (Tables S3 and S4) appear narrower than the bulk values but are the same within the error bars. Therefore, the overall spectral broadening (FWHM, Table 1) observed for the confined solutions is primarily due to inhomogeneous broadening, as discussed in Section 3.1. The increase in inhomogeneous broadening suggests that the increased variety of probe-solvent interactions that result in the broader linewidth arises from interactions introduced by confinement. These interactions also contribute to slower dynamics in the pores.

4. EFFECTS OF CONFINEMENT ON LIQUID DYNAMICS

4.1. Modified Two-State Models. In a two-state model for confined liquid behavior, a dynamical property, $D(t)$, assumes two distinct values corresponding to the "shell" and "core" states.[39,71] The shell state consists of molecules near the wall of the confining framework. Interactions of the shell molecules with the surface moieties typically result in shell dynamics differing from the bulk. The core state comprises molecules located near the pore center, away from the wall; the

https://doi.org/10.1021/acs.jpcb.4c01639
J. Phys. Chem. B 2024, 128, 5513−5527

core dynamics are often bulk-like. Systems may not strictly adhere to this binary classification, with intermediate layers of molecules between the wall and the pore center exhibiting a spectrum of dynamics spanning the extremes of shell-like and bulk-like. Modifications to the conventional two-state model can be used to accommodate more gradual transitions between core and shell behavior.

Modified two-state models have been successfully applied in previous dynamical studies of water[15] and MeIm[40] confined in mesoporous silica. The measured pore dynamics, $D(t)$, were modeled as a weighted sum of the core and shell dynamical components, $D_{core}(t)$ and $D_{shell}(t)$:[40]

$$D(t) = D_{core}(t) + [D_{shell}(t) - D_{core}(t)] \int_0^R m(\rho) \times f(\rho) d\rho \quad (5)$$

The variable R is the radius of the pore, and ρ corresponds to the radial distance from the center of the pore. The core dynamics, $D_{core}(t)$, are taken to be the measured bulk dynamics. The aim of fitting the spatially averaged pore data is to determine the width of the shell state and extract the shell dynamics, $D_{shell}(t)$, which cannot be directly measured.

The analytical weighting factor, $m(\rho)$, describes the spatial dependence of the core and shell behavior within a circular cross-section of a cylindrical pore. The proportion of shell behavior can be modeled to increase with increasing distance, ρ, from the pore center as a step function (eq 6), an exponential function (eq 7), or a smooth step function (eq 8):

$$m(\rho) = \theta[\Delta - (R - d_0 - \rho)] \quad (6)$$

$$m(\rho) = e^{-(R-d_0-\rho)/\xi} \quad (7)$$

$$m(\rho) = \frac{1}{2}\left(\tanh\left[\frac{\Delta - (R - d_0 - \rho)}{\alpha}\right] + 1\right) \quad (8)$$

The Heaviside step function in eq 6 describes a conventional two-state model with a variable parameter, Δ, which defines the position of the step at $\rho = R - d_0 - \Delta$ and corresponds to the thickness of the shell state. The reference value d_0 is defined and discussed in the SI. In the smooth step model in eq 8, Δ also defines the position of the step. Increasing α, the smoothness parameter, makes the transition between the shell and core states less abrupt. Conversely, as α approaches zero, eq 8 becomes a step function like eq 6. The exponential model in eq 7 describes a continuous acceleration of the dynamics with distance from the pore surface, with slow shell dynamics near the surface and faster, bulk-like dynamics at the pore center. This model is parametrized by a characteristic decay length, ξ.

Besides the core−shell transition in the liquid behavior represented by $m(\rho)$, the spatially averaged dynamics depend on the spatial distribution of the vibrational probe molecule reporting on the dynamics. In bulk solutions, the probe is uniformly distributed. This is not necessarily true in the pores. Molecular dynamics (MD) simulations were used in our previous studies[15,40] to determine the probability distribution of the probe molecules. Additional discussion of how those simulations informed the two-state model fitting is in the SI. The current study does not include simulations, which are difficult for aqueous electrolyte solutions and even more challenging for confined aqueous electrolyte solutions.[72,73] While simulation insight about nonuniform probe distributions can improve the fit quality, they are not necessary for obtaining meaningful information.

As reported in the MeIm study, using a conventional two-state model with a uniform $SeCN^-$ distribution produced a shell thickness comparable to that obtained with the more complex modified two-state models.[40] While the quality of the fits was not as good, the extracted shell dynamics and thicknesses were similar. For the water-associated dynamics in the 2.8 nm pore reported in another study,[15] using a uniform $SeCN^-$ distribution would result in shell dynamics and thickness similar to those from the reported fits informed by simulations. The simpler fits led to the same key conclusion: the thicker MeIm shell, which contained multiple MeIm molecules versus a shell of one water molecule, is associated with the more dramatic slowdown of MeIm versus water dynamics upon confinement. Thus, it should be reasonable to investigate the confinement effects on the aqueous $MgCl_2$ solutions using the two-state models with core−shell transitions described by eqs 6−8 and uniform $SeCN^-$ probability distributions. The shell thicknesses obtained will be compared with those for confined MeIm and water.

4.2. Core vs Shell Dynamics. Different dynamical variables in the same system can have different spatial dependencies. The core−shell transition for the confined $r(t)$ is best described by the exponential $m(\rho)$ given in eq 7, in agreement with previous studies on confined MeIm and water.[15,40] The spectral diffusion dynamics is best described by a sharp step (eq 6), like MeIm.[40] For water, a smooth step (eq 8) was more appropriate.[15] The fitting methodology was described in the MeIm study.[40] In short, to determine the combination of models that best reflects the data, independent and global fits of the anisotropy and spectral diffusion data sets for each concentration were performed using the three models (eqs 6−8). The relative quality of the fits with the different models was determined using the Akaike Information Criterion (AIC),[74] a widely used statistical method for comparing fitting models.

The modified two-state model fits (eq 7, exponential) to the $SeCN^-$ $r(t)$ in bulk (red) and confined (black) 1−16 $MgCl_2$-D_2O solutions are shown in Figure 5. The fits (eq 6, sharp step) for the CLS(T_w) are shown in Figure 6. The extracted shell correlation functions $D_{shell}(t)$ are shown with a dashed blue line. The shell correlation functions are the dynamics that would be observed if it were possible to make measurements on only the shell contributions. The shell $r(t)$ and CLS(T_w) were modeled with the minimum number of exponential decays necessary. The results are summarized in Tables 6 and 7.

4.2.1. Rotational Anisotropy, r(t). As shown in Table 6, the shell $r(t)$ extracted for the D_2O- and Mg^{2+}-associated peaks (for Mg^{2+}-associated, isolated using the two-component fits) are single exponential decays. This contrasts the multi-exponential bulk $r(t)$. Multiexponential $r(t)$'s are typically interpreted in terms of the wobbling-in-a-cone model of restricted orientational diffusion, in which following ultrafast inertial motions, restricted angular diffusion and, finally, complete orientational relaxation occur.[75−77] During the restricted angular diffusion process, the transition dipole (CN bond) samples an angular cone through "wobbling" motions. The dipole ultimately undergoes complete orientational randomization as solvent structural evolution relaxes the angular constraints. Since the shell $r(t)$'s are single exponential

https://doi.org/10.1021/acs.jpcb.4c01639
J. Phys. Chem. B 2024, 128, 5513−5527

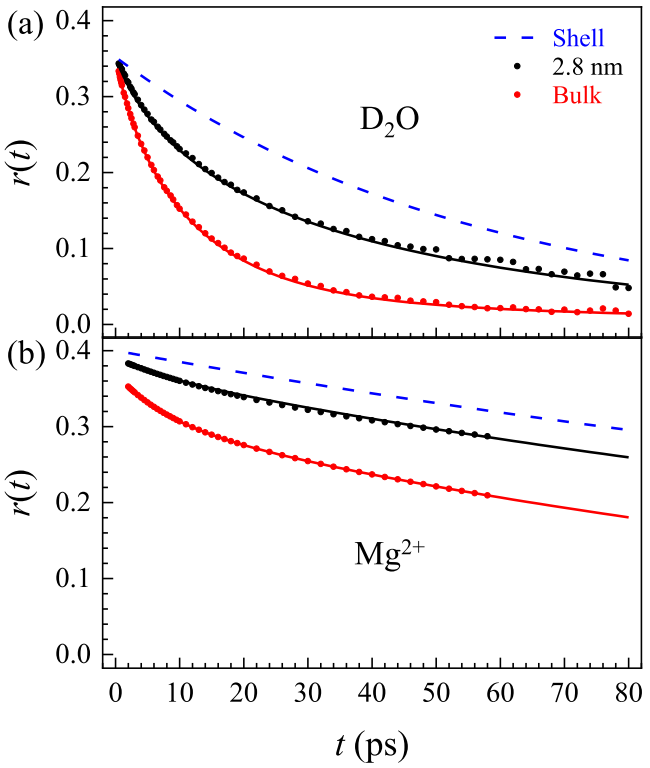

Figure 5. Measured rotational anisotropies $r(t)$ of $SeCN^-$ associated with (a) D_2O and (b) Mg^{2+} in bulk (red points) and confined (black points) 1−16 $MgCl_2$-D_2O solutions. The solid curves of the same colors are modified two-state model fits to the data. The blue dashed curves are the shell decays that yield the best fit to the experimental data.

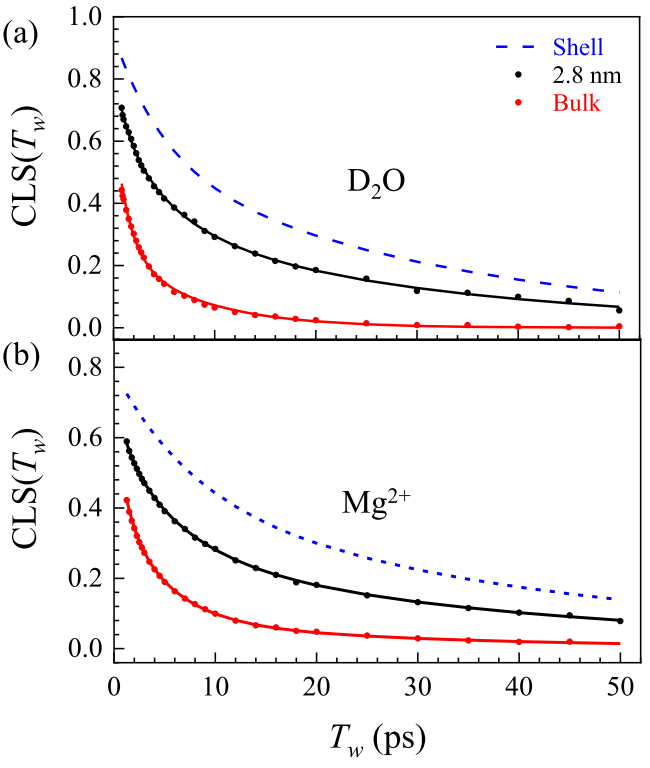

Figure 6. Measured CLS(T_w) decays (spectral diffusion) of $SeCN^-$ associated with (a) D_2O and (b) Mg^{2+} in bulk (red points) and confined (black points) 1−16 $MgCl_2$-D_2O solutions. The solid curves of the same colors are modified two-state model fits to the data. The blue dashed curves are the shell decays that yield the best fit to the experimental data.

decays, complete reorientation of the vibrational probe dominates the rotational dynamics at the surface. The wobbling motions present in the bulk are either very low in amplitude or do not occur at the surface.

Remarkably, for every concentration of $MgCl_2$ solution studied, the shell time constant (t_1) for the D_2O-associated peak is within error of the corresponding slowest time constant in the bulk (t_3) (compare Tables 2 and 6). For the 1−20 solution, the shell time constant is 38 ± 3 ps and the slowest bulk time constant is 39 ± 5 ps. However, the shell time constant (t_1) for the Mg^{2+}-associated peak is, depending on concentration, two to four times longer than the longest bulk time constant t_2 (compare Tables 3 and 6). For example, the 1−12 shell anisotropy time constant is 792 ± 75 ps, compared to 226 ± 27 ps in the bulk.

In hydrodynamic theory, the complete reorientation time is proportional to the solvent's bulk dynamic viscosity and the rotator's volume (vibrational probe) at a given temperature.[78−80] In the bulk study, we found that the Mg^{2+}-associated $SeCN^-$ exhibits hydrodynamic behavior and rotates as a unit with the Mg^{2+} hydration sphere, containing five water molecules at lower concentrations and three water molecules at the highest, 1−12 concentration.[38] The D_2O-associated $SeCN^-$ exhibits near-Debye diffusion behavior and rotates as a free anion. The slight deviation from Debye behavior results from hydrogen bond (H-bond) breakage and formation, or "jump" diffusion.[81]

The lack of change in the complete reorientation time for the D_2O-associated $SeCN^-$ in going from bulk (core) to shell suggests that neither the viscosity of the liquid nor the rotator

Table 6. Shell Orientational Dynamics from Two-State Model Fits[a]

	A_1	t_1 (ps)	ξ (Å)
	D_2O-associated		
1−12	0.361 ± 0.004	61 ± 4	7 ± 2
1−16	0.356 ± 0.006	56 ± 6	4.8 ± 0.5
1−20	0.36 ± 0.01	38 ± 3	3 ± 1
D_2O[b]	0.39 ± 0.01	14 ± 1	2.0[c]
	Mg^{2+}-associated		
1−12	0.393 ± 0.005	792 ± 75	5 ± 1
1−16	0.395 ± 0.008	274 ± 19	8 ± 1
1−20	0.399 ± 0.002	296 ± 31	9 ± 3

[a]Core dynamics were fixed to the bulk parameters (Tables 2 and 3) in the fits. For the Mg^{2+}-associated data, the Mg^{2+} dynamics isolated from the two-component fits were used. [b]ref 15. [c]No error bars were provided for the characteristic length, ξ, in the referenced publication.

volume changes. Conversely, the large change in the Mg^{2+}-associated complete reorientation time indicates a change in the viscosity or the volume of the Mg^{2+}-associated $SeCN^-$. One possibility involves the nature of the silica surface. In addition to silanol groups (Si−OH) at the pore surface, there are also Si−O groups. In the bulk solution, the Mg^{2+} cations do not form contact ion pairs with the chlorides.[82−84] However, in the pore, the Mg^{2+} cations can have strong electrostatic interactions with the immobile Si−O moieties, which have high charge densities, significantly slowing orientational relaxation. Additional shells of water may also be involved in the rotation of the Mg^{2+}-bound $SeCN^-$. Alternatively, there

https://doi.org/10.1021/acs.jpcb.4c01639
J. Phys. Chem. B 2024, 128, 5513−5527

Table 7. Shell Spectral Diffusion Dynamics from Two-State Model Fits[a]

	A_1	t_1 (ps)	A_2	t_2 (ps)	Δ (Å)
			D_2O-associated		
1−16	0.45 ± 0.08	4 ± 1	0.53 ± 0.08	37 ± 9	4.0 ± 0.4
1−20	0.6 ± 0.2	5 ± 1	0.4 ± 0.1	35 ± 19	3 ± 1
D_2O[b]	0.8 ± 0.04	1.9 ± 0.4	0.2 ± 0.05	14.6	2.8[c]
			Mg^{2+}-associated		
1−12	0.41 ± 0.05	7 ± 1	0.37 ± 0.07	58 ± 6	5 ± 2
1−16	0.37 ± 0.03	7 ± 2	0.44 ± 0.06	44 ± 8	4 ± 1
1−20	0.7 ± 0.2	5.3 ± 0.4	0.3 ± 0.1	51 ± 15	2 ± 1

[a]Core dynamics were fixed to the bulk parameters (Tables 4 and 5) in the fits. [b]ref 15. [c]A smoothed step function was used (vs sharp step) for the fits in the referenced publication, so an additional smoothness parameter α = 0.75 Å should be considered with the Δ parameter given.

may be local variations in the viscosity. The mechanisms of rotational diffusion may also be described by different boundary conditions[85,86] or perhaps involve dielectric friction[87,88] contributions due to the presence of charged and polar species in the charged silica pores.

The key is that confinement brings about different behaviors for the D_2O- and Mg^{2+}-associated probe species. Computational studies would be beneficial for identifying the specific structural changes arising from confinement that differentially alter the free and Mg^{2+}-bound components of the salt solution. For example, in a neutron diffraction study of bulk aqueous alkali salt solutions paired with computer simulations, the observed relative viscosity was correlated with a structural quantity, the average solute-water distance, and its deviation from the water−water distance in pure water.[89] A relevant conclusion from this study is that the change in the relative viscosity is not caused by changes in the bulk liquid, e.g., distortion of the H-bond network, but instead by the behavior of water molecules directly interacting with the alkali cation. In the present study, the relationship between the local environment of the Mg^{2+} solvation shell and viscosity may be enhanced by electrostatic interactions with the pore surface, inducing the differences in the shell dynamics of the D_2O- and Mg^{2+}-associated peaks.

4.2.2. Spectral Diffusion, CLS(T_w). The extracted shell correlation functions for spectral diffusion are biexponentials for both the D_2O- and Mg^{2+}-associated peaks (Table 7). Comparison of the amplitudes and time constants obtained for the bulk (Tables 4 and 5) and shell spectral diffusion reveals that spectral diffusion near the surface is characterized by slower time scales and that the slower spectral diffusion processes described by the slowest shell time constant, t_2, are weighted relatively more than the slowest bulk processes.

For the D_2O-associated peak, the shell time constants are many times larger than the corresponding bulk constants. For the bulk 1−16 solution (Table 4), the time constants are 1.4 and 8 ps. The corresponding shell time constants are 4 and 37 ps (Table 7). The interfacial time scales for $SeCN^-$ in confined D_2O were previously interpreted as slower analogs of the bulk components.[15] These bulk time scales correspond to local H-bond length and angle fluctuations (fast time scale) and randomization of the H-bond network (slow time scale).[58,60,69,90,91]

For the Mg^{2+}-associated peak, the shell correlation function (Table 7) is characterized by one fewer time constant than the bulk (Table 5). If the shell spectral diffusion time scales are slower analogs of the bulk, the two shell time scales may be much slower versions of the bulk t_1 and t_2 or slightly slower versions of the bulk t_2 and t_3 time constants. For the 1−16 solution, the bulk time constants are 1.2, 4.8, and 29 ps and the shell time constants are 7 and 44 ps. In the bulk, the Mg^{2+}-associated t_1 is equivalent to the D_2O-associated t_1, and this

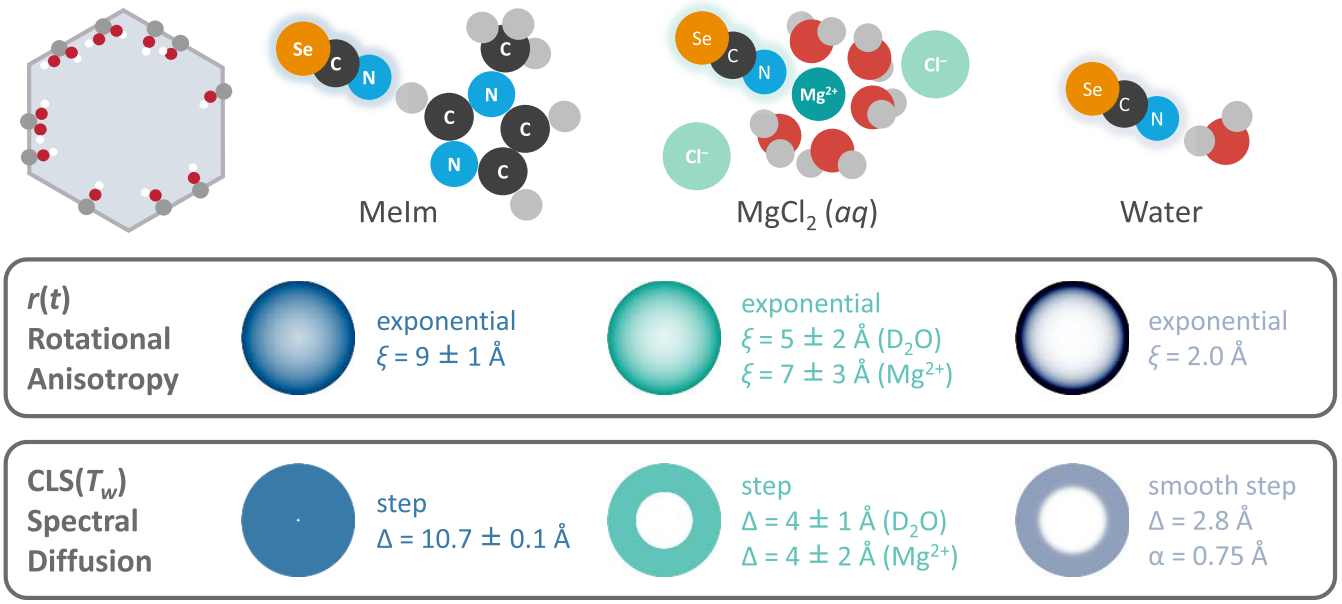

Figure 7. An illustration comparing the modified two-state model results for dynamics measured by $SeCN^-$ in MeIm, aqueous $MgCl_2$, and pure water confined in mesoporous silica. In the circular representations of the cross sections of the cylinder-like silica mesopores (cartoon of silica pore cross-section shown at top-left), darker colors represent greater shell state behavior and lighter colors represent greater core state behavior. The extent of surface effects, described by the parameters Δ and ξ, is greatest for MeIm and smallest for pure water. Note that for aqueous $MgCl_2$, only one cross-section is shown for both D_2O- and Mg^{2+}-associated dynamics, as the error bars for the parameters overlap.

https://doi.org/10.1021/acs.jpcb.4c01639
J. Phys. Chem. B 2024, 128, 5513−5527

fast time scale is associated with local H-bond fluctuations.[38] For the D_2O-associated peak, t_1 increases from ∼1 ps in the bulk to ∼4 to 5 ps in the shell. For the Mg^{2+}-associated peak, the first shell time constant, t_1, is ∼7 ps and may be a combination of two fast time constants with very similar decays. In this case, the Mg^{2+}-associated shell t_2 is the slower analog of the bulk t_3, and the slowdown upon confinement is a little less than a factor of 2.

Unlike the shell $r(t)$, which differs significantly for the D_2O- and Mg^{2+}-associated peaks, the shell CLS are quite similar for the two peaks. This similarity suggests that near the surface, the two species' spectral diffusion dynamics converge, with the D_2O-associated dynamics slowing significantly and the Mg^{2+}-associated dynamics becoming slightly slower.

4.3. Extent of Surface Effects and Different Liquids. Best fits (Figures 5 and 6) to the data support the use of the exponential and sharp step models for the rotational and spectral diffusion dynamics, respectively. This combination of models agrees well with our previous studies,[15,40] indicating that the analytical forms are meaningful at a molecular level. Note also that for an exponential model with a characteristic length equal to the step position of a sharp step model, the leading terms are the same for the corresponding expressions in the limit of uniform probe distributions and relatively large pore sizes.[39] In other words, equivalent length scales from different models describe a similar dependence on confinement, despite being based on different mathematical representations. The results of the two-state model fits for the D_2O- and Mg^{2+}-associated peaks are summarized in Tables 6 and 7, as well as in Figure 7. In the cross-sectional representations of a 2.8 nm pore (Figure 7), the color intensity, which represents shell behavior, decreases from the perimeter toward the center. The gradation visually illustrates the transition from the shell state (colored) to the bulk-like core state (white) according to the corresponding two-state models and length scales.

The exponential transition for the rotational anisotropy is described by a characteristic length, ξ (eq 7). In the three liquids we have studied in mesoporous silica: D_2O,[15] MeIm,[40] and aqueous $MgCl_2$ solutions, ξ is longest for MeIm at ∼9 Å and shortest for water at ∼2 Å, or roughly two layers of MeIm molecules and one layer of water molecules. See the first row in Figure 7 for the graphical representations. The ξ values for D_2O- and Mg^{2+}-associated dynamics in the $MgCl_2$ solutions, when averaged over all the concentrations, are 5 ± 2 and 7 ± 3 Å, respectively. As shown in Table 6, the values for the various concentrations differ but overlap when considering the error bars. Applying the Connolly solvent-excluded volume method[92] to the water molecules and the hexa-hydrated Mg^{2+} cations give respective molecular diameters of 2.7 and 6.1 Å. Accordingly, the ξ values are approximately two layers of water and one layer of a fully hydrated Mg^{2+} cation.

As discussed above, the Mg^{2+}-associated shell dynamics are significantly slower than the corresponding bulk dynamics, while the D_2O-associated shell dynamics have the same complete reorientation time as their bulk analogs. However, the ratio of the pore and bulk integrated correlation times τ_c is about two for both. For the 1−16 sample, the pore and bulk τ_c are 39 ps vs 18 ps for D_2O and 261 vs 124 ps for Mg^{2+}. In other words, the average confinement effect is not very different for the two species when considering the spatially averaged dynamics in 2.8 nm pores. Similarly, Martínez Casillas et al. found in their NMR and electrical conductivity studies that the diffusion mobilities of water and alkali cations confined in mesoporous silica are coupled, following the same trend with increasing confinement.[34] However, having decomposed the spatially averaged pore dynamics into shell and core components, we see that the Mg^{2+}-associated shell dynamics are impacted more by confinement. Martínez Casillas et al. also observed that in small silica pores <5 nm in diameter (c.f., 2.8 nm in the present study), cations with higher charge densities experience a more pronounced tortuosity effect due to stronger electrostatic interactions with the ionizable silanol surface groups. Thus, the impact for the ions is more significant than for water, as the latter interacts with the surface more weakly through H-bonds. Similarly, due to the high charge density of Mg^{2+}, the Mg^{2+}-associated shell dynamics deviate much more from the bulk than the water-associated shell dynamics. The difference in the shell dynamics must be considered alongside the extent of the surface effects, as described by ξ. The interplay of the two factors in different-sized pores ultimately governs the net confinement effects for the D_2O- and Mg^{2+}-associated dynamics.

The step model for the spectral diffusion describes a sharp change from shell to bulk-like dynamics. The parameter Δ describing the location of the step (eqs 6 and 8), or the shell thickness, like ξ for the rotational anisotropy, is again largest for MeIm (∼10.7 Å) and smallest for water (∼2.8 Å). The $MgCl_2$ Δ values (Table 7) are the same within error at the different concentrations and for the Mg^{2+}- and D_2O-associated peaks. The average Δ value is 4 Å, which is intermediate between the MeIm and water values and corresponds to one to two layers of water and a little less than a layer of a six-coordinated Mg^{2+} cation. The consistency in the Δ values is paralleled by similar, though not identical, shell CLS for the two peaks.

The distinct effects of confinement on the rotational and spectral diffusion dynamics highlight a fundamental difference in the two measurements. The anisotropy reported by the $SeCN^-$ probe is directly related to the probe behavior and indirectly influenced by the solvent dynamics. Meanwhile, the spectral diffusion of the CN vibrational frequency directly tracks time-dependent changes in the solvent structure. Spectral diffusion describes the more global behavior of a solvent system, reflecting the ensemble averaged intermolecular interactions and solvent fluctuations.

While the water- and cation-associated spectral diffusion dynamics differ in the bulk $MgCl_2$ solutions,[38] they become more similar near the pore surface. The shell time constants (t_1 and t_2) for the corresponding D_2O- and Mg^{2+}-associated peaks are identical within error (Table 7). This similarity suggests that the local environment of the D_2O-associated $SeCN^-$ probe becomes more like that of the Mg^{2+}-associated $SeCN^-$ near the pore surface. The similar extent of surface effects demonstrated by the spectral diffusion shell thickness of 4 Å for both the D_2O- and Mg^{2+}-associated $SeCN^-$ may indicate similar coordination behavior of the electrolyte species in the $MgCl_2$ solution, with both the Mg^{2+} and Cl^- ions coordinated to waters. Stabilization of the chloride hydration sphere relative to the bulk was previously observed in quasielastic neutron scattering studies of aqueous calcium chloride solutions confined in Vycor glass with 5 nm pores[93] and MCM-41 silica pores with 1.4−2.7 nm pores.[94] Restriction of water molecule motions near the chloride anions may result in the D_2O-associated $SeCN^-$ experiencing greater structural organ-

https://doi.org/10.1021/acs.jpcb.4c01639
J. Phys. Chem. B 2024, 128, 5513−5527

ization, thus requiring more degrees of freedom to randomize to sample the inhomogeneous line completely.

For the polar aprotic solvent we previously studied, MeIm, significant confinement effects were brought about by its large dipole moment.[40] In the bulk solution, because MeIm is aprotic, it does not form substantial H-bonds; therefore, the liquid is not highly structured. Upon confinement in mesoporous silica, the MeIm nitrogen lone pairs form H-bonds with the surface silanol groups. Subsequent electrostatic ordering of MeIm establishes antiparallel order extending two layers from the surface. The propagation of surface effects was evidenced by the shell length scales being on the order of a couple of MeIm molecules, in contrast to those for confined water,[15] which are roughly one water molecule (see Figure 7). The limited extent of surface effects for water was explained by the minor difference in the structural ordering of the amphiprotic molecule in the bulk and under confinement. Bulk water exhibits extensive structural ordering in the form of an H-bond network. Thus, H-bond interactions with the surface silanols have a limited effect on the structural order. For the aqueous salt solution presented in this study, the water- and cation-associated dynamics are described by length scales that are intermediate between those for MeIm and water. These length scales are generally on the scale of a couple of layers of water or a single layer of a hydrated ion.

The intermediate extent of shell behavior for the salt solution, compared to MeIm and water, is a reflection of the intermolecular interactions in the bulk $MgCl_2$ solution. While confinement only subtly affects the water H-bond network, confinement of the electrolyte solution in the charged silica pores alters the H-bonding among the water and ions, as well as the electrostatic interactions of the electrolyte species. The effects are, however, less pronounced than for MeIm, for which the confinement effect is dominated by electrostatic ordering.

5. CONCLUDING REMARKS

The ultrafast dynamics reported by the $SeCN^-$ vibrational probes in concentrated (2.5−4.2 molal) aqueous $MgCl_2$ solutions confined in MCM-41 silica with 2.8 nm diameter pores exhibit bulk-like concentration trends but are significantly slower than in the bulk. The linear absorption spectra, vibrational lifetimes, orientational relaxation, and spectral diffusion of the D_2O- and Mg^{2+}-associated $SeCN^-$ were measured using FT-IR, polarization selective pump−probe, and 2D IR spectroscopic techniques. The effects of confinement are intermediate between pure water and a polar aprotic solvent, MeIm, measured in the same pores.

The frequency shifts (or lack thereof) and broadening of the linear spectra with increasing salt concentration for the D_2O- and Mg^{2+}-associated peaks align with the bulk trends. Electrostatic interactions of the confined species with the charged silica surface can lead to altered and increased variety in probe-solvent interactions, resulting in broader (∼2−5 cm^{-1}) pore linewidths. These interactions may also enhance coupling and increase the density of states, or both, contributing to a slight decrease (∼2−5 ps) in the pore vibrational lifetimes. Surface interactions also drastically slow the rotational and spectral diffusion dynamics. Notably, the complete reorientation time is unchanged by confinement for the D_2O-associated species. In contrast, the complete reorientation time for the Mg^{2+}-associated species doubles in the pores. Upon confinement, the spectral diffusion dynamics become more similar for the two species.

The spatially averaged experimental data were decomposed into bulk-like core and slower shell dynamical contributions using modified two-state models. The extent and nature of the shell state vary depending on the liquid in the pore. The length scales that characterize the extent of the shell for the aqueous $MgCl_2$ solution are larger than those for confined water and smaller than those for confined MeIm. Considering that the intermolecular interactions in water are dominated by H-bonding and those in MeIm by dipole−dipole interactions, it seems reasonable that the $MgCl_2$ solution, involving both H-bonding and electrostatic interactions, would exhibit an intermediate response to confinement in the surface-charged silica pores. The different responses of the water- and cation-associated dynamics further illustrate the variation in confinement effects depending on the nature of the confined species.

The results presented here and the comparisons to other confined liquids underscore the differences in how confinement alters the structure and impacts the behavior of different liquids. Determining the confinement effects for $MgCl_2$ and other aqueous solutions can increase understanding of biological processes and aid the development of energy storage devices.

■ ASSOCIATED CONTENT

Supporting Information

The Supporting Information is available free of charge at https://pubs.acs.org/doi/10.1021/acs.jpcb.4c01639.

Discussion of filling the silica pores using a centrifuge. Cause and resolution for interfering pump−probe signals. Isotropic pump−probe signals. Two-component fits to anisotropy data. 2D Gaussian subtraction for 2D spectra. CLS decays in different polarization configurations. FFCF parameters. Considerations: nonuniform distribution of the vibrational probe and defining d_0 (PDF)

■ AUTHOR INFORMATION

Corresponding Author

Michael D. Fayer − *Department of Chemistry, Stanford University, Stanford, California 94305, United States;* orcid.org/0000-0002-0021-1815; Phone: (650) 723-4446; Email: fayer@stanford.edu

Authors

Samantha T. Hung − *Department of Chemistry, Stanford University, Stanford, California 94305, United States;* orcid.org/0000-0001-9448-0962

Sean A. Roget − *Department of Chemistry, Stanford University, Stanford, California 94305, United States;* orcid.org/0000-0003-2470-3571

Complete contact information is available at: https://pubs.acs.org/10.1021/acs.jpcb.4c01639

Notes

The authors declare no competing financial interest.

■ ACKNOWLEDGMENTS

This work was supported by the National Science Foundation, Division of Chemistry, award number 2319637. S.T.H. gratefully acknowledges partial support from an ARCS fellowship. Part of this work was performed at the Stanford

Nano Shared Facilities (SNSF), supported by the National Science Foundation under Award ECCS-2026822.

REFERENCES

(1) Videla, P. E.; Sala, J.; Martí, J.; Guàrdia, E.; Laria, D. Aqueous Electrolytes Confined within Functionalized Silica Nanopores. *J. Chem. Phys.* **2011**, *135*, No. 104503.
(2) Lynch, C. I.; Rao, S.; Sansom, M. S. Water in Nanopores and Biological Channels: A Molecular Simulation Perspective. *Chem. Rev.* **2020**, *120*, 10298−10335.
(3) Fraux, G.; Coudert, F.-X.; Boutin, A.; Fuchs, A. H. Forced Intrusion of Water and Aqueous Solutions in Microporous Materials: From Fundamental Thermodynamics to Energy Storage Devices. *Chem. Soc. Rev.* **2017**, *46*, 7421−7437.
(4) Wiggins, P. M. Role of Water in Some Biological Processes. *Microbiol. Mol. Biol. Rev.* **1990**, *54*, 432−449.
(5) Nierhaus, K. H. Mg^{2+}, K^{+}, and the Ribosome. *J. Bacteriol.* **2014**, *196*, 3817−3819.
(6) Flatman, P. W. Mechanisms of Magnesium Transport. *Annu. Rev. Physiol.* **1991**, *53*, 259−271.
(7) Wang, F.; Fan, X.; Gao, T.; Sun, W.; Ma, Z.; Yang, C.; Han, F.; Xu, K.; Wang, C. High-Voltage Aqueous Magnesium Ion Batteries. *ACS Cent. Sci.* **2017**, *3*, 1121−1128.
(8) Li, M.; Ding, Y.; Sun, Y.; Ren, Y.; Yang, J.; Yin, B.; Li, H.; Zhang, S.; Ma, T. Emerging Rechargeable Aqueous Magnesium Ion Battery. *Mater. Rep. Energy* **2022**, *2*, No. 100161.
(9) Burris, P. C.; Laage, D.; Thompson, W. H. Simulations of the Infrared, Raman, and 2D-IR Photon Echo Spectra of Water in Nanoscale Silica Pores. *J. Chem. Phys.* **2016**, *144*, No. 194709.
(10) Romero-Vargas Castrillón, S.; Giovambattista, N.; Aksay, I. A.; Debenedetti, P. G. Evolution from Surface-Influenced to Bulk-Like Dynamics in Nanoscopically Confined Water. *J. Phys. Chem. B* **2009**, *113*, 7973−7976.
(11) Milischuk, A. A.; Ladanyi, B. M. Structure and Dynamics of Water Confined in Silica Nanopores. *J. Chem. Phys.* **2011**, *135*, No. 174709.
(12) Laage, D.; Thompson, W. H. Reorientation Dynamics of Nanoconfined Water: Power-Law Decay, Hydrogen-Bond Jumps, and Test of a Two-State Model. *J. Chem. Phys.* **2012**, *136*, No. 044513.
(13) Bourg, I. C.; Steefel, C. I. Molecular Dynamics Simulations of Water Structure and Diffusion in Silica Nanopores. *J. Phys. Chem. C* **2012**, *116*, 11556−11564.
(14) Milischuk, A. A.; Ladanyi, B. M. Polarizability Anisotropy Relaxation in Nanoconfinement: Molecular Simulation Study of Water in Cylindrical Silica Pores. *J. Chem. Phys.* **2014**, *141*, No. 18C513.
(15) Yamada, S. A.; Hung, S. T.; Thompson, W. H.; Fayer, M. D. Effects of Pore Size on Water Dynamics in Mesoporous Silica. *J. Chem. Phys.* **2020**, *152*, No. 154704.
(16) Yuan, R.; Yan, C.; Nishida, J.; Fayer, M. D. Dynamics in a Water Interfacial Boundary Layer Investigated with IR Polarization-Selective Pump−Probe Experiments. *J. Phys. Chem. B* **2017**, *121*, 4530−4537.
(17) Chowdhary, J.; Ladanyi, B. M. Molecular Dynamics Simulation of Aerosol-OT Reverse Micelles. *J. Phys. Chem. B* **2009**, *113*, 15029−15039.
(18) Dokter, A. M.; Woutersen, S.; Bakker, H. J. Inhomogeneous Dynamics in Confined Water Nanodroplets. *Proc. Nat. Acad. Sci. U.S.A.* **2006**, *103*, 15355−15358.
(19) Piletic, I. R.; Moilanen, D. E.; Spry, D.; Levinger, N. E.; Fayer, M. Testing the Core/Shell Model of Nanoconfined Water in Reverse Micelles Using Linear and Nonlinear IR Spectroscopy. *J. Phys. Chem. A* **2006**, *110*, 4985−4999.
(20) Moilanen, D. E.; Fenn, E. E.; Wong, D.; Fayer, M. D. Water Dynamics in Large and Small Reverse Micelles: From Two Ensembles to Collective Behavior. *J. Chem. Phys.* **2009**, *131*, No. 014704.
(21) Pieniazek, P. A.; Lin, Y.-S.; Chowdhary, J.; Ladanyi, B. M.; Skinner, J. Vibrational Spectroscopy and Dynamics of Water Confined inside Reverse Micelles. *J. Phys. Chem. B* **2009**, *113*, 15017−15028.
(22) Singh, P. K.; Kuroda, D. G.; Hochstrasser, R. M. An Ion's Perspective on the Molecular Motions of Nanoconfined Water: A Two-Dimensional Infrared Spectroscopy Study. *J. Phys. Chem. B* **2013**, *117*, 9775−9784.
(23) Bakulin, A. A.; Cringus, D.; Pieniazek, P. A.; Skinner, J. L.; Jansen, T. L. C.; Pshenichnikov, M. S. Dynamics of Water Confined in Reversed Micelles: Multidimensional Vibrational Spectroscopy Study. *J. Phys. Chem. B* **2013**, *117*, 15545−15558.
(24) Moilanen, D. E.; Piletic, I. R.; Fayer, M. D. Water Dynamics in Nafion Fuel Cell Membranes: The Effects of Confinement and Structural Changes on the Hydrogen Bond Network. *J. Phys. Chem. C* **2007**, *111*, 8884−8891.
(25) Roget, S. A.; Kramer, P. L.; Thomaz, J. E.; Fayer, M. D. Bulk-Like and Interfacial Water Dynamics in Nafion Fuel Cell Membranes Investigated with Ultrafast Nonlinear IR Spectroscopy. *J. Phys. Chem. B* **2019**, *123*, 9408−9417.
(26) Beck, J. S.; Vartuli, J. C.; Roth, W. J.; Leonowicz, M. E.; Kresge, C.; Schmitt, K.; Chu, C.; Olson, D. H.; Sheppard, E.; McCullen, S. A New Family of Mesoporous Molecular Sieves Prepared with Liquid Crystal Templates. *J. Am. Chem. Soc.* **1992**, *114*, 10834−10843.
(27) Kresge, A. C.; Leonowicz, M. E.; Roth, W. J.; Vartuli, J.; Beck, J. Ordered Mesoporous Molecular Sieves Synthesized by a Liquid-Crystal Template Mechanism. *Nature* **1992**, *359*, 710−712.
(28) Martínez-Edo, G.; Balmori, A.; Pontón, I.; Marti del Rio, A.; Sánchez-García, D. Functionalized Ordered Mesoporous Silicas (MCM-41): Synthesis and Applications in Catalysis. *Catalysts* **2018**, *8*, 617.
(29) Pasricha, S.; Gahlot, P.; Mittal, K.; Rai, D.; Avasthi, N.; Kaur, H.; Rai, S. Functionalized MCM-41: Versatile Catalysts for Organic Transformations. *ChemistrySelect* **2022**, *7*, No. e202103674.
(30) Lee, C.-K.; Liu, S.-S.; Juang, L.-C.; Wang, C.-C.; Lin, K.-S.; Lyu, M.-D. Application of MCM-41 for Dyes Removal from Wastewater. *J. Hazard. Mater.* **2007**, *147*, 997−1005.
(31) Lu, D.; Xu, S.; Qiu, W.; Sun, Y.; Liu, X.; Yang, J.; Ma, J. Adsorption and Desorption Behaviors of Antibiotic Ciprofloxacin on Functionalized Spherical MCM-41 for Water Treatment. *J. Clean. Prod.* **2020**, *264*, No. 121644.
(32) Zeng, W.; Qian, X.-F.; Yin, J.; Zhu, Z.-K. The Drug Delivery System of MCM-41 Materials Via Co-Condensation Synthesis. *Mater. Chem. Phys.* **2006**, *97*, 437−441.
(33) Rámila, A.; Munoz, B.; Pérez-Pariente, J.; Vallet-Regí, M. Mesoporous MCM-41 as Drug Host System. *J. Sol-Gel Sci. Technol.* **2003**, *26*, 1199−1202.
(34) Martínez Casillas, D. C.; Longinotti, M. P.; Bruno, M. M.; Vaca Chávez, F.; Acosta, R. H.; Corti, H. R. Diffusion of Water and Electrolytes in Mesoporous Silica with a Wide Range of Pore Sizes. *J. Phys. Chem. C* **2018**, *122*, 3638−3647.
(35) Baum, M.; Rieutord, F.; Rébiscoul, D. Underlying Processes Driving the Evolution of Nanoporous Silica in Water and Electrolyte Solutions. *J. Phys. Chem. C* **2020**, *124*, 14531−14540.
(36) Osti, N. C.; Thapaliya, B. P.; Dai, S.; Tyagi, M.; Mamontov, E. Strong Enhancement of Nanoconfined Water Mobility by a Structure Breaking Salt. *J. Phys. Chem. Lett.* **2021**, *12*, 4038−4044.
(37) Baum, M.; Rieutord, F.; Juranyi, F.; Rey, C.; Rébiscoul, D. Dynamical and Structural Properties of Water in Silica Nanoconfinement: Impact of Pore Size, Ion Nature, and Electrolyte Concentration. *Langmuir* **2019**, *35*, 10780−10794.
(38) Hung, S. T.; Roget, S. A.; Zheng, W.; Fayer, M. D. Concentration Dependence of Dynamics and Structure among Hydrated Magnesium Ions: An Ultrafast Infrared Study. *J. Phys. Chem. B* **2023**, *127*, 3278−3290.
(39) Thompson, W. H. Perspective: Dynamics of Confined Liquids. *J. Chem. Phys.* **2018**, *149*, No. 170901.
(40) Hung, S. T.; Yamada, S. A.; Zheng, W.; Fayer, M. D. Ultrafast Dynamics and Liquid Structure in Mesoporous Silica: Propagation of Surface Effects in a Polar Aprotic Solvent. *J. Phys. Chem. B* **2021**, *125*, 10018−10034.

https://doi.org/10.1021/acs.jpcb.4c01639
J. Phys. Chem. B 2024, 128, 5513−5527

(41) Cheng, L.; Morrone, J. A.; Berne, B. J. Structure and Dynamics of Acetonitrile Confined in a Silica Nanopore. *J. Phys. Chem. C* **2012**, *116*, 9582−9593.
(42) Yamada, S. A.; Shin, J. Y.; Thompson, W. H.; Fayer, M. D. Water Dynamics in Nanoporous Silica: Ultrafast Vibrational Spectroscopy and Molecular Dynamics Simulations. *J. Phys. Chem. C* **2019**, *123*, 5790−5803.
(43) Greenspan, L. Water Activity Standards. *J. Res. Natl. Bur. Stand., Sect. A.* **1977**, *81*, 89−96.
(44) Swan, E. The Deliquescent Properties of Magnesium Chloride, of Calcium Chloride, and of Glycerol. *J. Text. Inst. Trans.* **1926**, *17*, T517−T526.
(45) Barrett, E. P.; Joyner, L. G.; Halenda, P. P. The Determination of Pore Volume and Area Distributions in Porous Substances. I. Computations from Nitrogen Isotherms. *J. Am. Chem. Soc.* **1951**, *73*, 373−380.
(46) Karthick Kumar, S.; Tamimi, A.; Fayer, M. Comparisons of 2D IR Measured Spectral Diffusion in Rotating Frames Using Pulse Shaping and in the Stationary Frame Using the Standard Method. *J. Chem. Phys.* **2012**, *137*, No. 184201.
(47) Tokmakoff, A. Orientational Correlation Functions and Polarization Selectivity for Nonlinear Spectroscopy of Isotropic Media. *I. Third Order. J. Chem. Phys.* **1996**, *105*, 1−12.
(48) Tan, H.-S.; Piletic, I. R.; Fayer, M. Polarization Selective Spectroscopy Experiments: Methodology and Pitfalls. *J. Opt. Soc. Am. B* **2005**, *22*, 2009−2017.
(49) Park, S.; Kwak, K.; Fayer, M. Ultrafast 2D-IR Vibrational Echo Spectroscopy: A Probe of Molecular Dynamics. *Laser Phys. Lett.* **2007**, *4*, 704.
(50) Hamm, P.; Zanni, M. T.; *Concepts and Methods of 2D Infrared Spectroscopy*; Cambridge University Press: New York, 2011.
(51) Shim, S.-H.; Strasfeld, D. B.; Fulmer, E. C.; Zanni, M. T. Femtosecond Pulse Shaping Directly in the Mid-IR Using Acousto-Optic Modulation. *Opt. Lett.* **2006**, *31*, 838−840.
(52) Shim, S.-H.; Zanni, M. T. How to Turn Your Pump−Probe Instrument into a Multidimensional Spectrometer: 2D IR and Vis Spectroscopies Via Pulse Shaping. *Phys. Chem. Chem. Phys.* **2009**, *11*, 748−761.
(53) Kwak, K.; Park, S.; Finkelstein, I. J.; Fayer, M. D. Frequency-Frequency Correlation Functions and Apodization in Two-Dimensional Infrared Vibrational Echo Spectroscopy: A New Approach. *J. Chem. Phys.* **2007**, *127*, No. 124503.
(54) Kwak, K.; Rosenfeld, D. E.; Fayer, M. Taking Apart the Two-Dimensional Infrared Vibrational Echo Spectra: More Information and Elimination of Distortions. *J. Chem. Phys.* **2008**, *128*, No. 204505.
(55) Hoffman, D. J.; Fayer, M. D. CLS Next Gen: Accurate Frequency−Frequency Correlation Functions from Center Line Slope Analysis of 2D Correlation Spectra Using Artificial Neural Networks. *J. Phys. Chem. A* **2020**, *124*, 5979−5992.
(56) Nishida, J.; Tamimi, A.; Fei, H.; Pullen, S.; Ott, S.; Cohen, S. M.; Fayer, M. D. Structural Dynamics inside a Functionalized Metal−Organic Framework Probed by Ultrafast 2D IR Spectroscopy. *Proc. Nat. Acad. Sci. U.S.A.* **2014**, *111*, 18442−18447.
(57) Donaldson, P. M.; Howe, R. F.; Hawkins, A. P.; Towrie, M.; Greetham, G. M. Ultrafast 2D-IR Spectroscopy of Intensely Optically Scattering Pelleted Solid Catalysts. *J. Chem. Phys.* **2023**, *158*, No. 114201, DOI: 10.1063/5.0139103.
(58) Yamada, S. A.; Thompson, W. H.; Fayer, M. D. Water-Anion Hydrogen Bonding Dynamics: Ultrafast IR Experiments and Simulations. *J. Chem. Phys.* **2017**, *146*, No. 234501.
(59) Schultz, P. Ab Initio Calculations of Ionic and Hydrogen Bonding Interactions with the OCN^- SCN^- and $SeCN^-$ Anions. *Mol. Phys.* **1996**, *88*, 217−246.
(60) Kramer, P. L.; Giammanco, C. H.; Fayer, M. D. Dynamics of Water, Methanol, and Ethanol in a Room Temperature Ionic Liquid. *J. Chem. Phys.* **2015**, *142*, No. 212408.
(61) Kenkre, V.; Tokmakoff, A.; Fayer, M. Theory of Vibrational Relaxation of Polyatomic Molecules in Liquids. *J. Chem. Phys.* **1994**, *101*, 10618−10629.
(62) Lenchenkov, V.; She, C.; Lian, T. Vibrational Relaxation of CN Stretch of Pseudo-Halide Anions (OCN^-, SCN^-, and $SeCN^-$) in Polar Solvents. *J. Phys. Chem. B* **2006**, *110*, 19990−19997.
(63) Li, S.; Shepherd, T. D.; Thompson, W. H. Simulations of the Vibrational Relaxation of a Model Diatomic Molecule in a Nanoconfined Polar Solvent. *J. Phys. Chem. A* **2004**, *108*, 7347−7355.
(64) Kramer, P. L.; Nishida, J.; Giammanco, C. H.; Tamimi, A.; Fayer, M. D. Observation and Theory of Reorientation-Induced Spectral Diffusion in Polarization-Selective 2D IR Spectroscopy. *J. Chem. Phys.* **2015**, *142*, No. 184505.
(65) Zheng, J.; Kwak, K.; Asbury, J.; Chen, X.; Piletic, I. R.; Fayer, M. D. Ultrafast Dynamics of Solute-Solvent Complexation Observed at Thermal Equilibrium in Real Time. *Science* **2005**, *309*, 1338−1343.
(66) Yuan, R.; Yan, C.; Fayer, M. Ion−Molecule Complex Dissociation and Formation Dynamics in LiCl Aqueous Solutions from 2D IR Spectroscopy. *J. Phys. Chem. B* **2018**, *122*, 10582−10592.
(67) Fenn, E. E.; Fayer, M. Extracting 2D IR Frequency-Frequency Correlation Functions from Two Component Systems. *J. Chem. Phys.* **2011**, *135*, No. 074502.
(68) Giammanco, C. H.; Kramer, P. L.; Fayer, M. D. Dynamics of Dihydrogen Bonding in Aqueous Solutions of Sodium Borohydride. *J. Phys. Chem. B* **2015**, *119*, 3546−3559.
(69) Yuan, R.; Fayer, M. D. Dynamics of Water Molecules and Ions in Concentrated Lithium Chloride Solutions Probed with Ultrafast 2D IR Spectroscopy. *J. Phys. Chem. B* **2019**, *123*, 7628−7639.
(70) Kubo, R.; *Fluctuation, Relaxation and Resonance in Magnetic Systems*; Oliver and Boyd: London, 1961.
(71) Norton, C. D.; Thompson, W. H. Reorientation Dynamics of Nanoconfined Acetonitrile: A Critical Examination of Two-State Models. *J. Phys. Chem. B* **2014**, *118*, 8227−8235.
(72) Panagiotopoulos, A. Z.; Yue, S. Dynamics of Aqueous Electrolyte Solutions: Challenges for Simulations. *J. Phys. Chem. B* **2023**, *127*, 430−437.
(73) Das, B.; Chandra, A. Ab Initio Molecular Dynamics Study of Aqueous Solutions of Magnesium and Calcium Nitrates: Hydration Shell Structure, Dynamics and Vibrational Echo Spectroscopy. *J. Phys. Chem. B* **2022**, *126*, 528−544.
(74) Akaike, H. A New Look at the Statistical Model Identification. *IEEE Trans. Autom. Control* **1974**, *19*, 716−723.
(75) Szabo, A.; Lipari, G. Model-Free Approach to the Interpretation of Nuclear Magnetic Resonance Relaxation in Macromolecules. 1. Theory and Range of Validity. *J. Am. Chem. Soc.* **1982**, *104*, 4546−4559.
(76) Kinosita, K., Jr; Kawato, S.; Ikegami, A. A Theory of Fluorescence Polarization Decay in Membranes. *Biophys. J.* **1977**, *20*, 289−305.
(77) Lipari, G.; Szabo, A. Effect of Librational Motion on Fluorescence Depolarization and Nuclear Magnetic Resonance Relaxation in Macromolecules and Membranes. *Biophys. J.* **1980**, *30*, 489−506.
(78) Sension, R. J.; Hochstrasser, R. M. Comment On: Rotational Friction Coefficients for Ellipsoids and Chemical Molecules with Slip Boundary Conditions. *J. Chem. Phys.* **1993**, *98*, 2490−2490.
(79) Youngren, G.; Acrivos, A. Rotational Friction Coefficients for Ellipsoids and Chemical Molecules with the Slip Boundary Condition. *J. Chem. Phys.* **1975**, *63*, 3846−3848.
(80) Moog, R.; Ediger, M.; Boxer, S.; Fayer, M. Viscosity Dependence of the Rotational Reorientation of Rhodamine B in Mono-and Polyalcohols. Picosecond Transient Grating Experiments. *J. Phys. Chem.* **1982**, *86*, 4694−4700.
(81) Laage, D.; Hynes, J. T. Reorientional Dynamics of Water Molecules in Anionic Hydration Shells. *Proc. Nat. Acad. Sci. U.S.A.* **2007**, *104*, 11167−11172.
(82) Callahan, K. M.; Casillas-Ituarte, N. N.; Roeselová, M.; Allen, H. C.; Tobias, D. J. Solvation of Magnesium Dication: Molecular Dynamics Simulation and Vibrational Spectroscopic Study of Magnesium Chloride in Aqueous Solutions. *J. Phys. Chem. A* **2010**, *114*, 5141−5148.

(83) Larentzos, J. P.; Criscenti, L. J. A Molecular Dynamics Study of Alkaline Earth Metal−Chloride Complexation in Aqueous Solution. *J. Phys. Chem. B* **2008**, *112*, 14243−14250.
(84) Pye, C. C.; Rudolph, W. An Ab Initio and Raman Investigation of Magnesium (II) Hydration. *J. Phys. Chem. A* **1998**, *102*, 9933−9943.
(85) Hu, C. M.; Zwanzig, R. Rotational Friction Coefficients for Spheroids with the Slipping Boundary Condition. *J. Chem. Phys.* **1974**, *60*, 4354−4357.
(86) Perrin, F. Mouvement Brownien D'un Ellipsoide-I. Dispersion Diélectrique Pour Des Molécules Ellipsoidales. *J. Phys. Radium* **1934**, *5*, 497−511.
(87) Zwanzig, R. Dielectric Friction on a Moving Ion. *J. Chem. Phys.* **1963**, *38*, 1603−1605.
(88) Hubbard, J. B. Dielectric Dispersion and Dielectric Friction in Electrolyte Solutions. *II. J. Chem. Phys.* **1978**, *68*, 1649−1664.
(89) Corridoni, T.; Mancinelli, R.; Ricci, M.; Bruni, F. Viscosity of Aqueous Solutions and Local Microscopic Structure. *J. Phys. Chem. B* **2011**, *115*, 14008−14013.
(90) Asbury, J. B.; Steinel, T.; Stromberg, C.; Corcelli, S.; Lawrence, C.; Skinner, J.; Fayer, M. Water Dynamics: Vibrational Echo Correlation Spectroscopy and Comparison to Molecular Dynamics Simulations. *J. Phys. Chem. A* **2004**, *108*, 1107−1119.
(91) Asbury, J. B.; Steinel, T.; Kwak, K.; Corcelli, S.; Lawrence, C.; Skinner, J.; Fayer, M. Dynamics of Water Probed with Vibrational Echo Correlation Spectroscopy. *J. Chem. Phys.* **2004**, *121*, 12431−12446.
(92) Connolly, M. L. Computation of Molecular Volume. *J. Am. Chem. Soc.* **1985**, *107*, 1118−1124.
(93) Mamontov, E.; Cole, D. R. Quasielastic Neutron Scattering Study of Dynamics of $CaCl_2$ Aqueous Solution Confined in Vycor Glass. *Phys. Chem. Chem. Phys.* **2006**, *8*, 4908−4914.
(94) Mamontov, E.; Cole, D. R.; Dai, S.; Pawel, M. D.; Liang, C.; Jenkins, T.; Gasparovic, G.; Kintzel, E. Dynamics of Water in LiCl and $CaCl_2$ Aqueous Solutions Confined in Silica Matrices: A Back-scattering Neutron Spectroscopy Study. *Chem. Phys.* **2008**, *352*, 117−124.

https://doi.org/10.1021/acs.jpcb.4c01639
J. Phys. Chem. B 2024, 128, 5513−5527